Cell Reports

Article

Stochastic models of nucleosome dynamics reveal regulatory rules of stimulus-induced epigenome remodeling

Graphical abstract

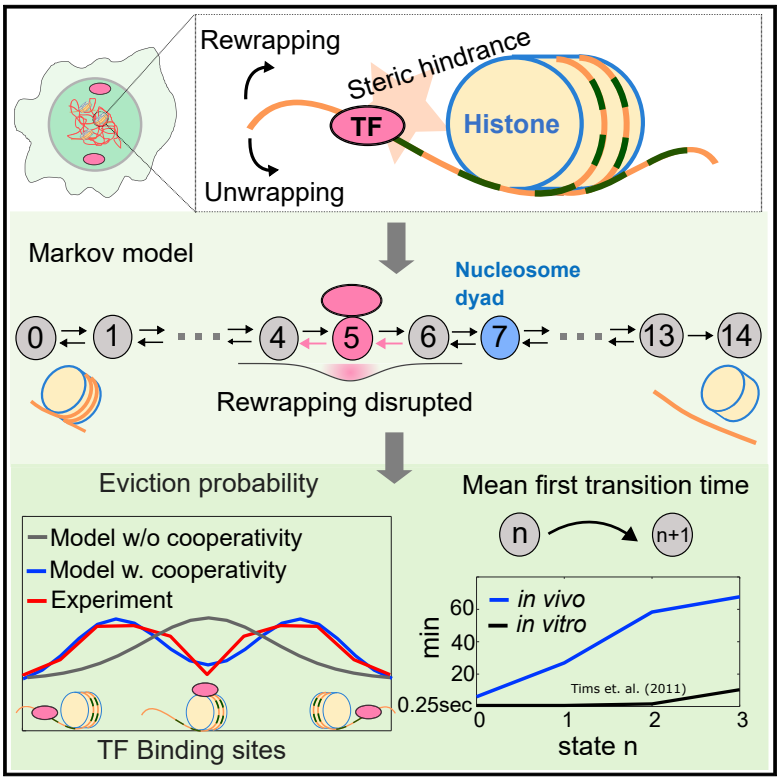

Highlights

- Markov models of nucleosome-SDTF interactions fit stimulus response ATAC-seq data
- In cells, unwrapping may occur in minutes, rather than seconds, as in *in vitro*
- Models reveal cooperativity and estimate an SDTF effect range of 30–40 bp
- SDTF sites close to but not on the dyad evict nucleosomes with greatest likelihood

Authors

Jinsu Kim, Katherine M. Sheu, Quen J. Cheng, Alexander Hoffmann, German Enciso

Correspondence

enciso@uci.edu (G.E.), ahoffmann@ucla.edu (A.H.)

In brief

Kim et al. examine regulatory principles governing transcription factor-induced nucleosome eviction by analyzing Markov models fit to genome-wide chromatin accessibility measurements. Fitted models reveal nucleosome unwrapping rates, cooperativity of unwrapping steps, and why nucleosome eviction probability is highest when transcription factor binding sites are adjacent to the nucleosome dyad.

Kim et al., 2022, Cell Reports *40*, 111076
July 12, 2022
https://doi.org/10.1016/j.celrep.2022.111076

CellPress

Cell Reports

CellPress
OPEN ACCESS

Article

Stochastic models of nucleosome dynamics reveal regulatory rules of stimulus-induced epigenome remodeling

Jinsu Kim,[1,7] Katherine M. Sheu,[2,3,7] Quen J. Cheng,[2,4] Alexander Hoffmann,[2,3,8,*] and German Enciso[5,6,8,9,*]
[1]Department of Mathematics, Pohang University of Science and Technology, Pohang, South Korea
[2]Department of Microbiology, Immunology, and Molecular Genetics, University of California, Los Angeles, Los Angeles, CA, USA
[3]Institute for Quantitative and Computational Biosciences, University of California, Los Angeles, Los Angeles, CA, USA
[4]Department of Medicine, Division of Infectious Diseases, University of California, Los Angeles, Los Angeles, CA, USA
[5]Department of Mathematics, University of California, Irvine, Irvine, CA, USA
[6]Department of Developmental and Cell Biology, University of California, Irvine, Irvine, CA, USA
[7]These authors contributed equally
[8]Senior author
[9]Lead contact
*Correspondence: enciso@uci.edu (G.E.), ahoffmann@ucla.edu (A.H.)
https://doi.org/10.1016/j.celrep.2022.111076

SUMMARY

The genomic positions of nucleosomes are a defining feature of the cell's epigenomic state, but signal-dependent transcription factors (SDTFs), upon activation, bind to specific genomic locations and modify nucleosome positioning. Here we leverage SDTFs as perturbation probes to learn about nucleosome dynamics in living cells. We develop Markov models of nucleosome dynamics and fit them to time course sequencing data of DNA accessibility. We find that (1) the dynamics of DNA unwrapping are significantly slower in cells than reported from cell-free experiments, (2) only models with cooperativity in wrapping and unwrapping fit the available data, (3) SDTF activity produces the highest eviction probability when its binding site is adjacent to but not on the nucleosome dyad, and (4) oscillatory SDTF activity results in high location variability. Our work uncovers the regulatory rules governing SDTF-induced nucleosome dynamics in live cells, which can predict chromatin accessibility alterations during inflammation at single-nucleosome resolution.

INTRODUCTION

Nucleosomes are critical for packaging the eukaryotic genome into the nucleus: 2 m of human DNA must be packed into a 1-μm nucleus (Alberts et al., 2002). As a consequence of packing, access to the DNA is limited, but selective access is important for gene expression (Allfrey et al., 1963). Hence, nucleosomes have evolved to be highly dynamic. Dynamic nucleosome repositioning, including histone assembly, disassembly, and eviction, are important for generating dynamic chromatin states that are ultimately permissive or non-permissive to gene expression (Lee et al., 2004; Shivaswamy et al., 2008).

Early biophysical *in vitro* studies of histone octamer-DNA interactions focused on high-resolution studies of static interactions (culminating in X-ray or cryoelectron microscopy [cryo-EM] structures) as well as dynamic interactions of nucleosomal DNA sequences bound to reconstituted histones in cell-free experimental systems (Zhou et al., 2019). High-resolution structures elucidated the interaction points between the histone octamer (H2A-H2B pairs and H3-H4 pairs) and the DNA wrapped around it (Luger et al., 1997). *In vitro* studies of nucleosome unwrapping and rewrapping determined with a variety of methods, including fluorescence resonance energy transfer (FRET), revealed quantities such as the average time taken for spontaneous DNA unwrapping (Li et al., 2005), the differences in timescales of dissociation and reassociation of the different DNA-histone contact regions on the nucleosome (Tims et al., 2011), and a fundamental asymmetry in the process so that the unwrapping of one side helped to stabilize the other side (Ngo et al., 2015).

Mathematical models have explored the dynamic behavior of nucleosomes and their role in chromatin biology, including the effect of chromatin remodeling proteins on nucleosome sliding (Chou, 2007) and the deposition of histone marks along nucleosome arrays for epigenetic memory (Dodd et al., 2007). Nucleosomes have also been modeled with biophysical accuracy by incorporating the nucleosomal structure of 14 DNA-histone contact points and describing how DNA unwrapping/rewrapping depends on particular rate parameters (Cheng et al., 2021; Dobrovolskaia and Arya, 2012; Möbius et al., 2006). These theoretical approaches show that mathematical models, especially those involving Markov chains and Brownian motion, can be used to reproduce *in vitro* experimental measurements and to provide insights such as an analytic form of the mean DNA

detachment time, DNA bending angles, and bistability in histone modifications.

However, little is known about nucleosome dynamics as they occur on native chromatin in living cells. These "*in vivo*" dynamics are likely markedly different from dynamics measured in cell-free systems "*in vitro*" because the interactions between DNA polymer and histone octamer are constrained and because additional protein factors that are not present in biochemical studies may further stabilize or destabilize the nucleosome. For example, linker histones present *in vivo* also bind to nucleosomal core particles close to the DNA entry and exit sites, and enzymatic machines such as SWI/SNF (SWItch/Sucrose Non-Fermentable) (Dechassa et al., 2010) or FACT(FAcilitates Chromatin Transcription) complexes facilitate nucleosome repositioning (Chen et al., 2018; Liu et al., 2020). However, we know little about these dynamics quantitatively because there has not been a straightforward way to measure nucleosome positioning *in vivo* and no controlled way to perturb steady-state positions.

Two recent advances have allowed us to probe nucleosome dynamics. First, next-generation sequencing (NGS) has provided ways to measure nucleosome accessibility and positioning with DNase1 and, more recently, with the assay for transposase-accessible chromatin (ATAC-seq). These genome-wide measurements revealed that nucleosome positions *in vivo* are to a large degree determined by DNA sequence (Segal and Widom, 2009; Segal et al., 2006). Second, identification of DNA-binding proteins called pioneer factors, which may displace nucleosomes by competing with histones for DNA contacts, provides a means to perturb nucleosomes. The discovery that stimulus-induced signal-dependent transcription factors (SDTFs) may also initiate nucleosome re-positioning now allows them to be used as a probe to study *in vivo* dynamics because they provide a trigger to perturb DNA-histone interactions within the cell at controllable start times (Ostuni et al., 2013; Sen et al., 2020; Weinmann et al., 1999). In particular, the dynamics of inflammation-activated SDTF activity has been shown to determine the propensity for nucleosome repositioning in macrophages and fibroblasts (Cheng et al., 2021; Sen et al., 2020). This suggests that SDTF activation with stimulus-specific dynamics may be used as a probe to study the histone-DNA interaction dynamics in the nucleosome via NGS measurements at stimulus start and endpoints.

Here we present stochastic models for epigenetic remodeling, which, in this paper, refers to changes in chromatin accessibility. These math models are based on structural features of the nucleosome to investigate the regulatory rules behind nucleosome eviction. Using probability theory, we calculated the probability of histone eviction and the resulting mean chromatin accessibility under various dynamical SDTF signaling patterns. We report that oscillatory SDTF signals potentially induce greater variability of cell fate in heterogeneous cell environments than constant SDTF signals. Then, by experimentally tracking nucleosomes at different genomic locations and counting the number of nucleosome evictions between two time points, we found that optimal eviction takes place when the SDTF binds adjacent to the dyad, defined as the center position of nucleosomal DNA, rather than directly on top of it, indicative of the cooperativity of histone-DNA contacts. Thus, our modeling approach allows us to derive quantitative insights from NGS chromatin accessibility data; provides a framework for understanding location-specific, SDTF-induced chromatin accessibility changes in different cellular contexts; and constitutes a tool to predict eviction probability for single nucleosomes in live cells responding to inflammation.

RESULTS

A stochastic model accounts for nucleosome dynamics upon SDTF binding *in vivo*

When SDTFs bind to DNA, their stimulus-specific temporal dynamics disrupt the resting state distribution of nucleosomes, affecting chromatin accessibility (Figure 1A). Epigenetic dynamics can be modeled as a continuous system; for example, deterministic ordinary differential equation models describing chromatin accessibility in bulk have been used to describe chromatin opening steps that result in enhancer formation (Cheng et al., 2021). However, DNA unwrapping/rewrapping of individual nucleosomes is subject to molecular stochasticity. The binding of SDTFs to DNA can be regarded as a time-dependent on/off switch dramatically influencing chromatin dynamics; this binding is discrete and stochastic. To incorporate such noisy behavior and discreteness, we used a continuous-time, discrete-state Markov chain to model chromatin accessibility with time-dependent SDTF binding. This model is time inhomogeneous because the transitions given by SDTF binding/unbinding are time dependent (STAR Methods).

To reflect the biophysical structure of the nucleosome, we assumed that each nucleosome consists of 14 stepwise unwrapping and rewrapping transitions, consistent with structural data on the number of contact points between the histone and DNA (Luger et al., 1997), as well as previous nucleosome unwrapping models (Figure 1B; Cheng et al., 2021; Mobius et al., 2013). Approximately 147 bp of DNA wrap one and three-quarter times around the core histone octamer (Luger et al., 2012), resulting in 14 main non-covalent DNA-histone contact points (Luger et al., 1997). To fully displace the nucleosome from any particular genomic location, multiple steps may be required. Hence, based on structural and biophysical measurements performed on single nucleosomes *in vitro*, we used a coupled stochastic process $(X(t),N(t))$, where $X(t)$ represents the number of disassembled DNA-histone contact regions, and $N(t)$ takes either 0 or 1 to represent the on/off state of the SDTF binding (Figure 1C). We considered the spontaneous, stepwise unwrapping behavior of DNA from a single histone, which originates at the locations furthest from the nucleosome dyad (state 7).

Regarding the symmetry of the model, we assumed a one-sided unwrapping model where DNA unpacks from state 0. Prior experimental cryo-EM or atomic force microscopy studies have investigated whether the nucleosome unwraps from one side at a time or two sides simultaneously. The results suggested that one-sided unwrapping is more likely because opening of one nucleosomal end stabilizes the other end (de Bruin et al., 2016; Konrad et al., 2021; Mauney et al., 2018). In addition, structural studies of the H1 linker histone have shown that the H1 globular domain bound directly on the dyad and associated with both

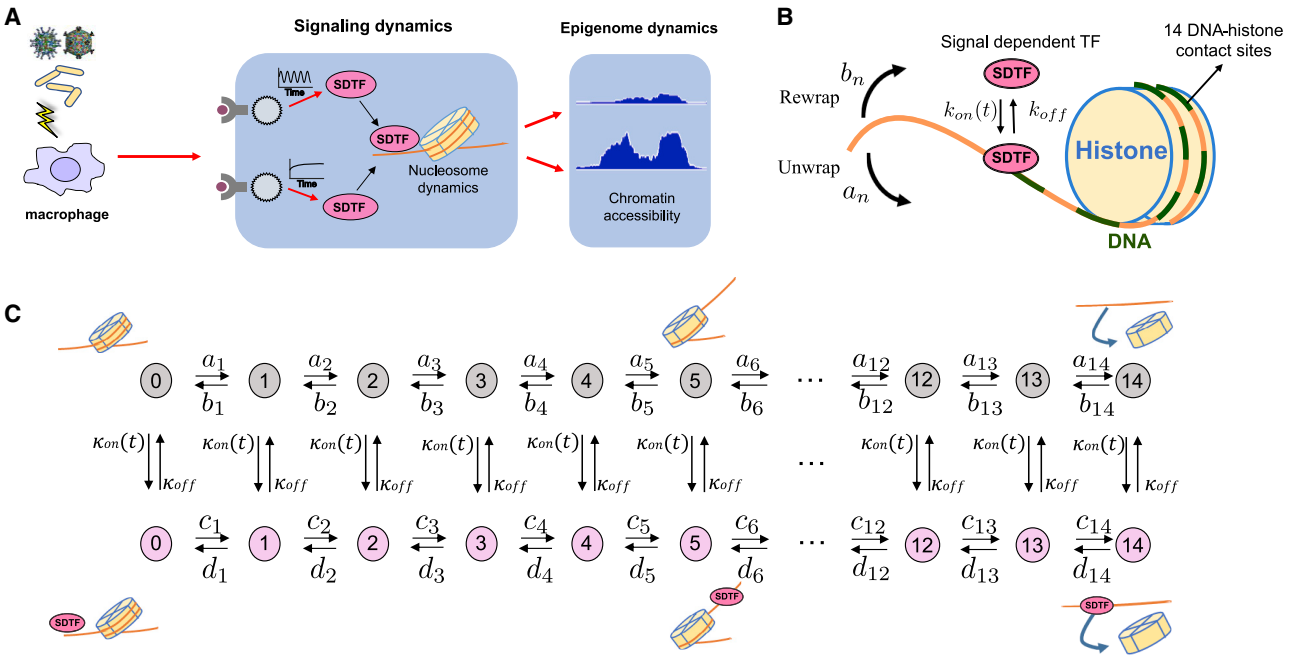

Figure 1. A stochastic model accounts for nucleosome eviction by dynamic SDTF activity

(A) Immune responses activate SDTFs with different temporal dynamics, ultimately affecting chromatin accessibility.

(B) Schematic for the unwrapping/rewrapping model for nucleosome dynamics under SDTF signaling dynamics.

(C) State configuration of the stochastic nucleosome model, where a_i, b_i, c_i, d_i represent rate parameters.

See also Figures S1 and S7.

sides of the linker DNA, whereas the H1 C-terminal domain attached to just one of the two linker DNA segments (Bednar et al., 2017). We surmised that the asymmetry of linker histones may also further promote one-sided asymmetrical unwrapping *in vivo*. Although unwrapping and wrapping of the nucleosome is primarily unidirectional (Bilokapic et al., 2018; Li et al., 2005; Ngo et al., 2015), we also considered and analyzed the possibility that it takes place simultaneously at both ends of the DNA (STAR Methods; Figure S1), and we found that the qualitative behavior of 1-sided and 2-sided stochastic models were similar. Hence, we settled on using the 1-sided model in the main results of this paper.

The amount of energy released by re-establishing hydrogen bonds between histone and DNA is greater than the energy released by the straightening of the DNA polymer during unwrapping, so the rates of rewrapping exceed that of unwrapping, which, in our model, corresponds to setting $a_i < b_i$ (Tims et al., 2011). We set the unwrapping/rewrapping parameters as $a_n = a_1 h^{n-1}[min^{-1}]$ and $b_n = b_1 h^{-n+1}[min^{-1}]$ with a cooperativity constant h so that DNA unwraps more easily the more unwrapped it already is. Biophysical and structural measurements on single nucleosomes support the cooperative and multistep transitions in DNA unwrapping from the histone (Li et al., 2005; Polach and Widom, 1995; Tims et al., 2011), but the extent of such cooperativity remains a free parameter that can be later fit to data. We note that evidence of cooperativity in the literature is measured in isolated nucleosomes *in vitro*, whereas our measurements were carried out in the full cellular chromatin environment.

We then considered the effect of a dynamic signaling protein that competes for DNA binding with the histone core octamer. Short periods of DNA accessibility may be stabilized by the binding of transcription factors when their cognate binding sequence is present in that stretch of DNA and they are present at sufficiently high concentrations (Klemm et al., 2019). Spontaneous nucleosome dynamics, also known as nucleosome breathing, allow transient exposure of nucleosomal DNA, and the binding of SDTFs provides steric hindrance that occludes the rewrapping of DNA-histone contacts in the nucleosome. The on-state of the SDTF makes the nucleosome rewrapping parameter d_n much less than b_n around the SDTF binding site (Figure 1C), whereas c_n is set to be identical to a_n. When a histone is fully evicted, it detaches entirely from the DNA and might not dock again to the same genomic location. Thus, we assumed that $b_{14} = d_{14} = 0$ so that state 14 is an absorbing state of $X(t)$. That is, if $X(s) = 14$ for some s, then $X(t) = 14$ for all $t > s$. We also analyzed the alternative assumption that state 14 is non-absorbing, which represents reattachment of an evicted histone, and found that the models produced similar behavior (STAR Methods).

It is known that transcription factor binding operates at a faster timescale than DNA wrapping or unwrapping (Callegari et al., 2019). Hence for a given SDTF concentration $f(t)$, we used the SDTF binding rate $\kappa_{on}(t) = cf(t)$ with a large constant c, and the unbinding rate κ_{off} is proportional to $\kappa_{on}(0)$. Indeed, the stochastic system behaves almost identically with any choice of large c, and this is shown in the STAR Methods using a timescale decomposition argument. For large values of c, the ratio

$BF = \kappa_{off}/(\kappa_{on} + \kappa_{off})$ approximately determines the fraction of time the SDTF is unbound. The ratio BF could depend on time when the SDTF signal is oscillatory, and it can also depend on the strength of the SDTF input.

In another difference from previous models, we considered the SDTF binding position in relation to the original nucleosome dyad. Because the nucleosome encompasses ~147 bp of DNA, and SDTF binding motifs typically stretch 8–10 bp (Stewart et al., 2012), the stochastic binding and unbinding of the SDTF from DNA at the site of its motif is modeled with genome location-specific resolution by incorporating the relative location of binding motifs from the nucleosome dyad. When the SDTF binds to its cognate motif, it tends to disrupt DNA-histone contacts in its vicinity. The effect of SDTF binding on the rewrapping parameter is highest near the SDTF binding site and decreases with distance. See STAR Methods and Table S1 for a mathematical derivation of statistical quantities, the definition of the parameters, and the choice of parameter values of the stochastic process $(X(t), N(t))$

Periodicity of SDTF oscillations affects DNA accessibility

In inflammation signaling, the importance of signaling dynamics is well appreciated (Behar and Hoffmann, 2010; Purvis and Lahav, 2013; Werner et al., 2005). A prominent SDTF that is activated during immune responses is nuclear factor κB (NF-κB). For NF-κB signaling, the amplitude (Lee et al., 2014) and duration (Hoffmann et al., 2002; Sen et al., 2020) of the signal controls which genes are activated. However, only recently has the importance of oscillatory versus non-oscillatory signaling been revealed in remodeling the epigenome (Cheng et al., 2021) rather than in primary response gene expression (Barken et al., 2005). Previously published experimental systems involving mutations of NF-κB feedback regulators allowed comparison of oscillatory (wild-type [WT]) and non-oscillatory (Mut) NF-κB activity after tumor necrosis factor (TNF) stimulation of macrophages (Figure 2A; Adelaja et al., 2021; Cheng et al., 2021), but there is currently no experimental system that allows altering the period of NF-κB oscillations (Longo et al., 2013). Thus, we used the stochastic model to examine how the period of SDTF oscillations alters chromatin accessibility; we analyzed the results of numerical computations with the probability distribution of the full histone eviction time.

The period of the oscillation quantitatively affects the time-course dynamics of chromatin accessibility. We set the cooperativity constant $h = 1.3$, and we set the unwrapping/rewrapping parameters as $a_n = 0.2h^{n-1}$, $b_n = 3h^{-n+1}$ for each state n in the stochastic nucleosome model. For simplicity, we used zero rewrapping rates under the SDTF binding, meaning $d_n = 0$ at each state n. We considered two oscillatory SDTF inputs of 10 min and 60 min half-periods, respectively, that have the same aggregate signal within the time interval $[0, 500]$ min (Figure 2B). We sampled 50 time courses of our stochastic model under each of these two oscillatory inputs, using the Extrande method (Voliotis et al., 2016), which is a stochastic simulation algorithm for Markov chains with time-dependent transition rates. The rapid oscillatory SDTF signal with a half-period of 10 min unwrapped the nucleosome completely in 19 of 50 samples within 500 min, whereas 40 of 50 samples were fully unwrapped by 500 min when the half-period was 60 min (Figure 2C). This result reflected experimental results where SDTF dynamics of longer continuous duration resulted in increased nucleosome eviction (Cheng et al., 2021).

To further analyze this system modeled under the two different dynamic SDTF signals, we described the DNA wrapping process as a "success or failure game" (Figures S2A–S2C), which can be analyzed with a geometric distribution. In the case of a cooperative system with $h = 1.3$, when $X(t)$ reaches state 6 or above, the unwrapping parameters a_{n+1} are greater than the rewrapping parameters b_n so that $X(t)$ can easily reach state 14 (state of full eviction) even without the support of SDTF binding. Hence, success of $X(t)$ is reaching state 6, and we used the probability of the success to analyze the distinct behaviors of DNA under two oscillatory inputs.

If nucleosomes are exposed to an SDTF signal at amplitude 10 for 10 min, then only about 2. 5% of nucleosomes reach state 6 (Figure S2C). Hence, during the on-phase (i.e., SDTF signal at amplitude 10), nearly 2.5% of DNA segments can successfully unwrap from the entire histone octamer under this rapid oscillation. After the first 10 min of oscillation, when the SDTF signal is turned off, most remaining nucleosomal DNA that failed to reach state 10 during the previous on-phases, rapidly rewraps around the histone because the rewrapping parameter b_n is much greater than the unwrapping parameter a_n for $n < 6$, likely returning back to state 0. Therefore, in the next on-phase, about 2.5% of the remaining free DNA can be fully unwrapped, and DNA undergoes this process 25 times by 500 min. This "success or failure game" under the oscillatory SDTF signal can be described using the geometric distribution $Geo(0.025)$ with a success probability of 0.025 (Figures S2A and S2B). Similarly, the full eviction probability by 500 min under the SDTF signal of 60 min half-period can be estimated with $Geo(0.24)$ because the success probability is about 24% during the 60 min on-phase. The full eviction probabilities computed with the geometric distributions $Geo(0.025)$ and $Geo(0.24)$ are about 0.47 and 0.7, respectively, which closely estimate the actual eviction probabilities shown in Figure 2D. The detailed computations of the full eviction probabilities using these two geometric distributions are shown in STAR Methods.

In our simulations, very fast oscillations of the SDTF signal did not necessarily render the DNA less accessible. Indeed, when the half-period was 0.3 s, the SDTF signal is interpreted as a constant signal with half the amplitude. Therefore, despite the extremely short on-phase of the oscillation, about 50% of DNA temporal trajectories were fully unwrapped by 500 min (Figure 2C bottom), which is higher than when the half-period was 10 min. Intuitively, this phenomenon occurs because the optimal scenario for the least unwrapping is based on the SDTF oscillation frequency matching the relative unwrapping/rewrapping frequency of the nucleosome. The time evolutions of histone eviction probability under these three different SDTF signals are displayed in Figure 2D. See STAR Methods and Figure S2 for more detailed mathematical analysis about the full eviction probability under different frequencies of the SDTF signal.

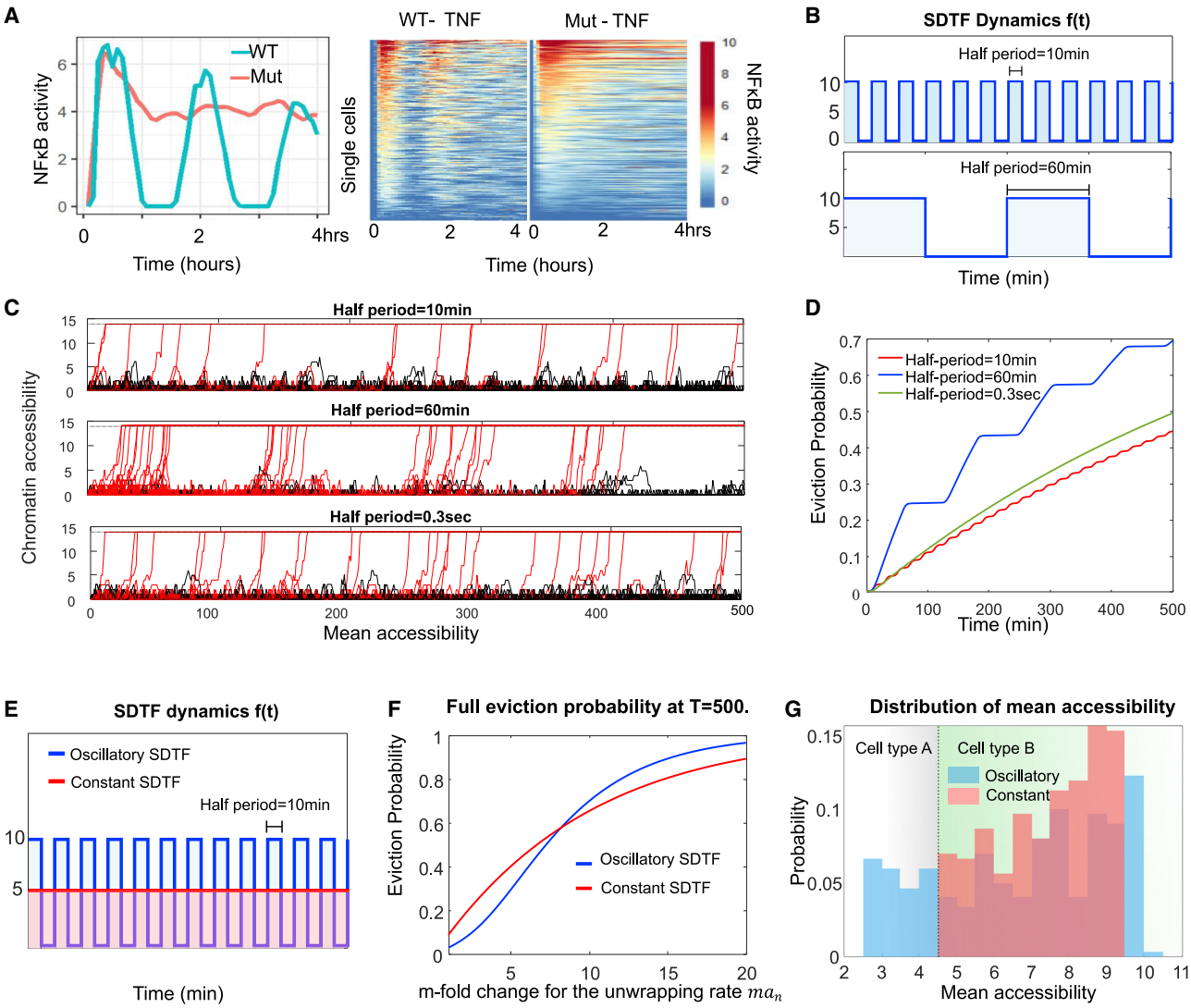

Figure 2. Periodicity of SDTF oscillations affects DNA accessibility

(A) Experimental knowledge of SDTF signaling dynamics in single cells (left: two individual single cells; right: hundreds of single cells). Color bar represents fluorescence of nuclear NF-κB. WT and Mut cells activate NF-κB with different temporal dynamics (Adelaja et al., 2021).

(B–D) Chromatin response to oscillatory SDTF dynamics with different frequency.

(B) SDTF dynamics with rapid (top) or slow oscillation (bottom).

(C) 50 sample traces of DNA dynamics under the oscillatory SDTF inputs of half-period = 10 min (top) and 60 min (bottom). Red traces reach the fully evicted state, and black traces do not.

(D) Time evolution of histone eviction probability.

(E–G) Parameter sensitivity under oscillatory versus constant SDTF signals.

(E) Oscillatory and constant SDTF signal inputs.

(F) Full eviction probability versus unwrap parameter cooperativity (h = 1.3). m represents the fold change increase in unwrapping/rewrapping parameters.

(G) Mean chromatin accessibility distribution at t = 500 min with the oscillatory or constant SDTF dynamics. To model heterogeneous cell environment, we randomly perturb the system parameters. Coefficient variation (standard deviation/mean) of the distributions under oscillatory SDTF and constant SDTF is 0.35 and 0.12, respectively.

See also Figure S2.

Oscillatory SDTF inputs can lead to heterogeneous chromatin accessibility responses

Although our computational investigation of different SDTF oscillatory frequencies cannot be tested in experimental systems (because the period is hardwired by the IκBα-NF-κB negative feedback loop; Longo et al., 2013), we now considered that the same oscillatory SDTF dynamics may affect different nucleosomes in a cell differently because of differences in kinetic parameters determined by location-specific molecular mechanisms.

To explore the capacity for differential responses of various chromatin regions to the same dynamic signal, we scanned the nucleosome unwrapping/rewrapping parameters and computed the probability of histone eviction using the stochastic model under non-oscillatory or oscillatory inputs with a fixed period (Figure 2E). We found that the system was more sensitive to the unwrapping/rewrapping parameters under oscillatory than non-oscillatory SDTF dynamics (Figure 2F). We used the same parameters as used in previous simulations, and they are shown in Table S1.

Under oscillatory and constant SDTF dynamics, we calculated the probability of histone eviction at T = 360 min after multiplying each of the unwrapping/rewrapping parameters a_n and b_n by a fold change parameter m (Figure 2F). Under oscillatory SDTF dynamics, the full DNA eviction probability rapidly grows for $m \in [2,4]$. In fact, this graph has a sigmoidal shape, indicative of a higher sensitivity with respect to fold change increases, so that the same oscillatory input can lead to widely different responses for different parameter values. In the STAR Methods, using simple matrix exponentials, we explored sensitivity analysis with our stochastic model under constant transition rates and time-dependent oscillatory transition rates.

We may speculate that the greater variability of chromatin accessibility under an oscillatory SDTF input allows more cell-to-cell variability of cell fate decisions. For instance, if the cell type is determined by a threshold mean accessibility at particular chromatin regions, then an oscillatory SDTF may produce type A and type B, whereas a non-oscillatory SDTF may more consistently convert cells to type B (Figure 2G).

Eviction probability profiles characterize the *in vivo* nucleosome unwrapping process

We next sought to use the nucleosome model to investigate how the location of the SDTF binding site relative to each nucleosome might affect nucleosome eviction. We utilized ATAC-seq data from an IκBα knockout mutant macrophage experimental system (Cheng et al., 2021) at a 0-h baseline and 4 h after NF-κB had been activated by TNF stimulation. Using paired-end ATAC-seq to separate nucleosomal read fragments from nucleosome-free read fragments, we calculated nucleosome dyad positions across the genome (Schep et al., 2015; Figure S3). We assessed nucleosome dyad locations relative to κB sites before and after stimulation and observed a reduction in the number of κB site-associated nucleosomes after NF-κB activation, but this reduction depended on the distance between the κB site and the nucleosome dyad (Figure 3A).

To understand why the location of the binding motif relative to nucleosome dyad position affects nucleosome eviction, we added mechanistic detail to the nucleosome model. We allowed the rewrapping parameters to depend on the SDTF binding site location along the 147-bp stretch of DNA that encompasses the nucleosome. Hence, DNA locations within a certain range around the SDTF binding site have a rewrapping parameter d_n that is smaller than b_n. For simplicity we used a Gaussian formula, which allowed us to center the effect at the SDTF binding site and control the range of its influence. We used the formula $d_n = b_n(1 - \exp(-(s-n)^2/2\sigma^2))$, where s is the SDTF binding location, and the standard deviation σ represents the SDTF effect range (Figure 3B). In this way, $d_n \approx b_n$ for a state n far from the binding site s, and $d_n \approx 0$ when n is close to s (Figure 3C).

In the nucleosome model, the unwrapping and rewrapping parameters may describe cooperativity within the unwrapping mechanism, meaning that every unwrapping step facilitates further unwrapping (i.e., a_n increases and b_n decreases in n). If the system is non-cooperative, then each state n has constant parameters a_n and b_n. Prior evidence suggests that the unwrapping process may be highly cooperative, either because of an inherent cooperativity of contact points within the nucleosome or because of the collaborative mechanism between DNA binding proteins that promote nucleosome eviction (Miller and Widom, 2003). To achieve such behavior, the unwrapping and rewrapping parameters were modeled as $a_n = a_1 h^{n-1}$ and $b_n = b_1 h^{-n+1}$ for each n with cooperativity constant h. The special case of $h = 1$ indicates non-cooperative behavior.

Although the unwrapping parameters are increasing, the average timescales for site exposure from state n to state $n+1$, or from state 0 to state n, still become progressively longer, as observed experimentally (Tims et al., 2011). This is because the opening process from state n to state $n+1$ could involve multiple steps of unwrapping and rewrapping. For example, one possible trajectory of DNA from state 5 to state 6 consists of the path $5 \rightarrow 4 \rightarrow 3 \rightarrow 4 \rightarrow 5 \rightarrow 6$ (STAR Methods).

We then tested which binding location is optimal for nucleosome eviction under constant SDTF activity. SDTF binding motifs were distributed across the DNA strand in the range [−100 bps, 100 bps] centered at the histone dyad (state 7 in Figure 3B). We assumed that the SDTF binds at one of the states s in {−3,−2, …,16,17}, which is an extended range from the original state space {0,1, …,14} (Figure 1C), so that we can consider SDTF binding motifs lying slightly outside the nucleosome. Then, for each distance relative to the nucleosome dyad, computed as $|7-s| \times 10$ (bp), we calculated the full eviction probability. The resulting behaviors under various levels of cooperativity of the parameters a_n and b_n are distinct because the optimal binding site is either in the center of the nucleosome or toward the extremes. Under non-cooperative rates $(h = 1)$, the optimal binding site is at the nucleosome dyad so that the full eviction probability is symmetric about the relative distance between the SDTF binding site and dyad (Figure 3D). In contrast, when the parameters model cooperative behavior $(h > 1)$, the optimal site is closer to the unwrapping edge, and, hence, the full eviction graph has a peak close to this edge (Figure 3E left). This is because when the first few contacts between DNA and histone are unwrapped, the cooperativity of the system facilitates unwrapping of the remainder. After averaging multiple cells, because of the symmetry of nucleosomes unwrapping from either end, the probability-binding site plot has a center dip (Figure 3E, right). Given such different patterns of eviction probability versus the distance of the SDTF binding site from the dyad, we termed the graph the "eviction probability profile" and concluded that it may be used to characterize the *in vivo* nucleosome unwrapping process. In STAR Methods and Figure S4, we provide a mathematical analysis of the effect of the SDTF binding site on the probability of nucleosome eviction.

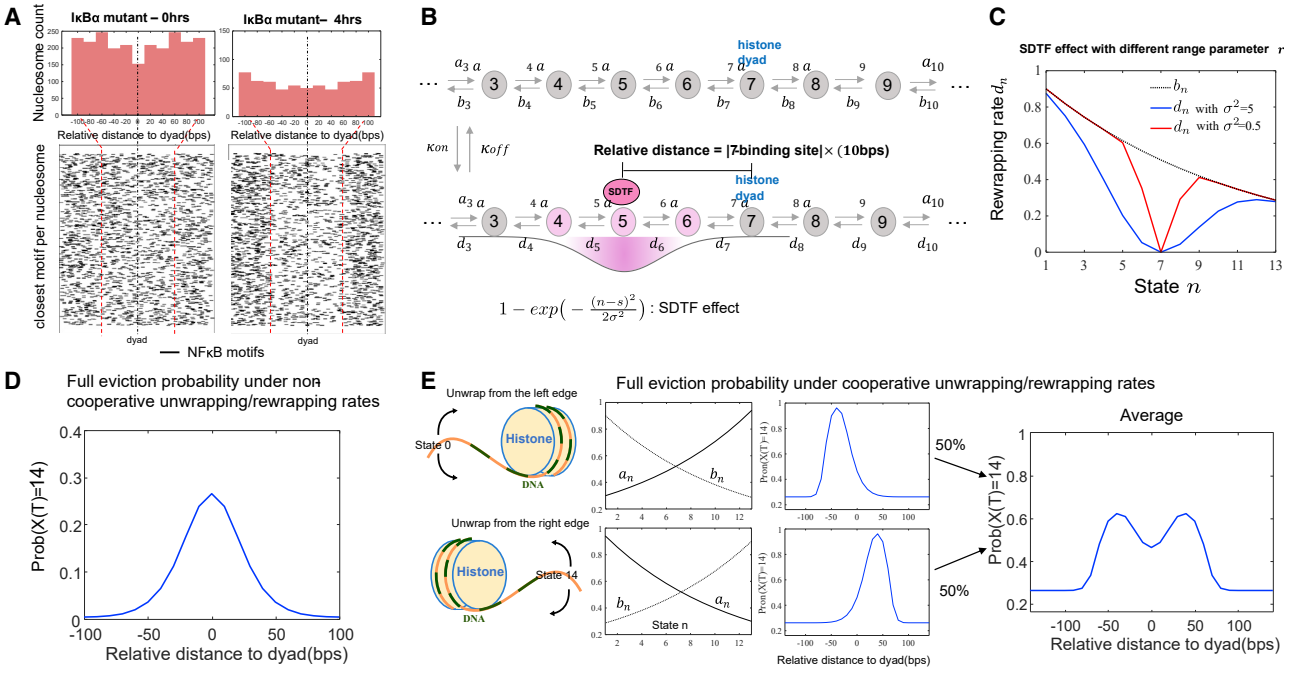

Figure 3. Modeling SDTF binding sites, range of SDTF effect, and cooperativity in unwrapping steps reveals potential eviction probability profiles

(A) Summary of NF-κB motifs adjacent to nucleosome dyads. Shown are NF-κB motifs in relation to each nucleosome dyad called by NucleoATAC (Schep et al., 2015) 0 h and 4 h after TNF stimulation in male mouse bone marrow-derived macrophages (BMDMs) (no replicates used, n = 1 for each time point, validation experiment performed in Figure 6). Locations shown have an NF-κB motif ±100 bp of the nucleosome dyad.

(B) SDTFs locally affects the DNA-histone contact regions near the SDTF binding site.

(C) The range parameter σ determines how widely the SDTF affects the rewrapping parameters.

(D) Computation of the full eviction probability via the stochastic model shows that motifs at the dyad promote greater nucleosome unwrapping probability under a non-oscillatory SDTF signal and non-cooperative open/close parameters.

(E) The full eviction probability is maximal at the SDTF binding location between the edge and dyad under cooperative unwrap/rewrap parameters. Assuming 50% of right edge unwrapping and 50% of left edge unwrapping, the average full eviction probability displays a center valley.

See also Figures S3, S4, and S6.

The model predicts cooperativity based on eviction probability profiles

The shape of the eviction probability profile is altered not only by wrapping cooperativity (parameter *h*) but also by the range of the SDTF binding effect (parameter σ), which is likely to be SDTF specific. If the range is wider, then all rewrapping parameters d_n are equally affected so that the probability plot becomes more flattened. We first examined computationally how different values of the cooperativity parameter *h* and the SDTF range parameter σ could alter chromatin accessibility (Figure 4A). We tested multiple potential values of this range parameter as well as cooperativity parameters $h = 1$ (non-cooperative), 1.1, and 1.2 (high cooperativity). We also used $\sigma^2 = 2.5$, 10 and 50 for the range of the SDTF binding effect. It is notable that, for higher cooperativity and narrower SDTF binding effect range, the plot of full DNA eviction probability displays a clearer center valley.

Using this relation between the model parameters and the eviction probability profile, we next compared these computational results with experimental measurements. We fit model parameters to data on nucleosome eviction probabilities given the SDTF binding motif location relative to the dyad. The parameter σ corresponds to the standard deviation of the Gaussian curve describing the influence of the SDTF binding, in units of number of binding sites. Because these binding sites are approximately 10 base pairs away from each other, a value of $\sigma = 2$ would correspond to a standard deviation of around 20 bp or a range of 40 bp around the SDTF binding site.

We returned to the time-course experimental data from macrophages responding to TNF stimulation (Figure 3A). Because ATAC-seq data can provide an estimate of the nucleosome positions, we assigned nucleosomes to their nearest TSS at the baseline time point 0 h and tracked whether the nucleosomes matching the same TSS changed in position or disappeared at the later time point of 4 h, quantified by having fewer or no nucleosomes mapping to that TSS (STAR Methods). Using the difference of the nucleosome counts between two time points, we computed experimental full nucleosome eviction probability for each relative motif distance by 240 min after TNF stimulation as

$$\mathrm{Prob}(X(240) = 14) = 1 - \mathrm{Prob}(X(240)<14) \approx 1 - \frac{\#\ of\ nucleosome\ at\ 4hr}{\#\ of\ nucleosome\ at\ 0hr}.$$

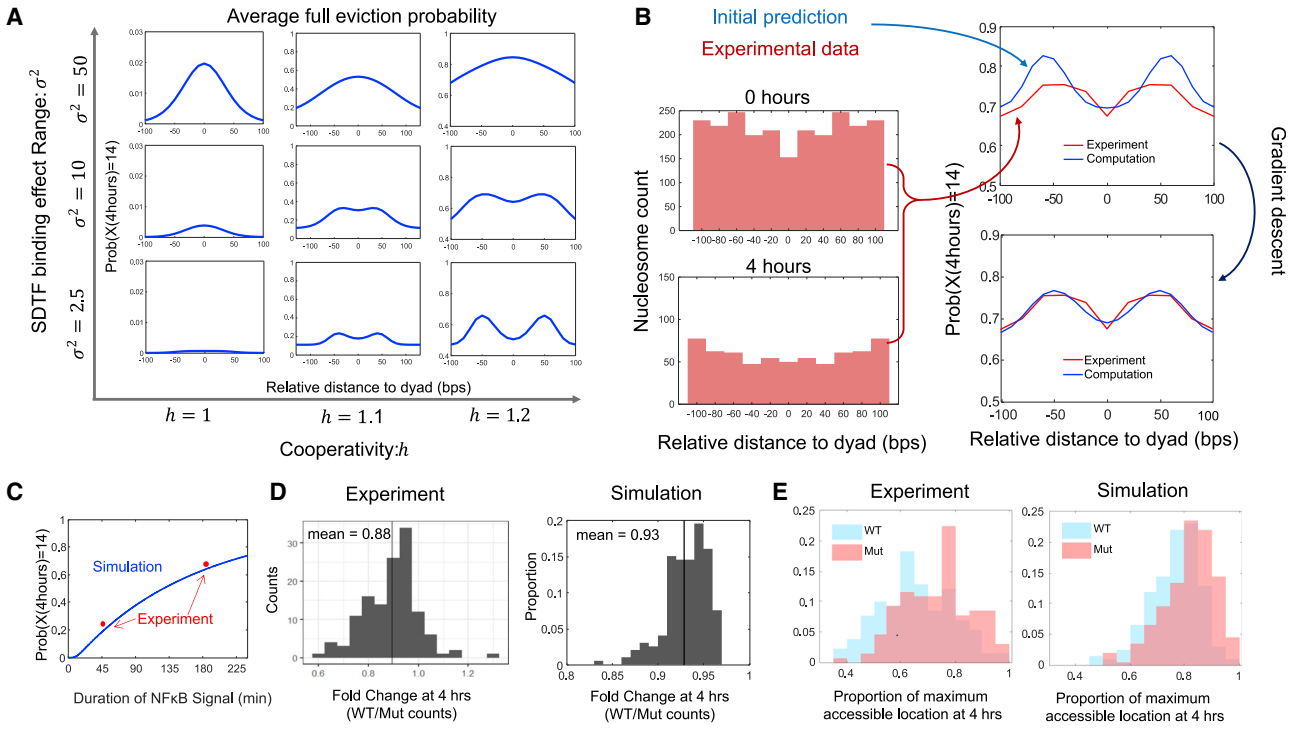

Figure 4. Fitting the model eviction probability profiles to SDTF binding location data provides evidence of cooperativity and estimates model parameters

(A) Probabilities of full eviction with respect to relative motif position from the nucleosome dyad and SDTF binding effect range for the macrophage system under a non-oscillatory NF-κB signal. Three different ranges (σ^2 = 1.5, 10, and 50) and cooperativity parameters (h = 1, 1.1 and 1.2) are chosen.

(B) Left: nucleosome counts from male mouse BMDM ATAC-seq samples under non-oscillatory TNF-induced NF-κB activity at NF-κB motifs at 0 h and 4 h (no replicates used, n = 1 for each time point, validation experiment performed in Figure 6). Right: full eviction probability versus SDTF binding locations. Shown are the experiment-based eviction probability profile (red curves) and model-based eviction probability profile before and after parameter fitting by gradient descent (blue curves).

(C) Full DNA eviction probability under a steady NF-κB input signal of different durations. Red: experimental measurements shown in Cheng et al. (2021). Blue: simulated values using the stochastic model with the fitted parameters in Table S1.

(D) Left: fold change (WT/Mut) of resulting chromatin accessibility after activation of SDTFs with different dynamics. Two biological replicates were used for each genotype (n = 2). Right: reproduction of the experimental measurements using the stochastic nucleosome model under the fitted parameters listed in Table S1. Counts are converted to proportion because of simulation of a different number of nucleosome locations.

(E) Left: variance in chromatin accessibility across genomic locations at 4 h in WT and Mut cells, as measured by bulk ATAC-seq. Two biological replicates were used for each genotype (n = 2). Right: reproduction of the experimental measurements using the stochastic nucleosome model.

See also Figure S5.

We used these data to fit values of the different parameters in our model by approximating an initial set of parameters, followed by gradient descent (Courant, 1994) to find the optimal parameter set. Fitted parameters included the cooperativity parameter, SDTF range parameter, unwrapping/rewrapping parameters, and SDTF binding/unbinding rates. For IκBα knockout macrophages treated with TNF for 4 h (Cheng et al., 2021), fitting these parameters resulted in the best-fit eviction probability profile (Figure 4B; see STAR Methods for additional details and Table S1 for the resulting parameter values.) Based on the shape of the fitted eviction probability profile, we found that the nucleosome unwrapping/rewrapping parameters are likely cooperative. The range of SDTF effect was fitted at σ = 2.1, which corresponds to a radius of around 20 bp from the SDTF binding site or 40 bp around the binding site. The initial unwrapping parameter a_1 = 0.16 indicates that the first DNA unwrapping from the fully wrapped configuration takes approximately $1/0.161$ = 6.25 min on average. See Figure S5 for an analysis of the error between the eviction probability profiles of the data and the model. Recent studies have shown that nucleosome eviction is likely to take place under a long NF-κB signal pulse of approximately 120 min but that it rarely occurs under a shorter NF-κB signal pulse of less than 45 min (Cheng et al., 2021), and similar observations have been made in fibroblasts after 60 min and 150 min, respectively (Sen et al., 2020). These observations can be reproduced with our stochastic model under the fitted parameters (Figure 4C).

To further compare the model with experimental data, we examined several properties of the chromatin locations. We hypothesized that the ATAC-seq distributions across genomic locations in WT and Mut macrophages could be reproduced by simulating the stochastic model using the fitted parameters. Indeed, under fitted parameter values (Table S1), simulations of the stochastic model reproduced two experimental findings

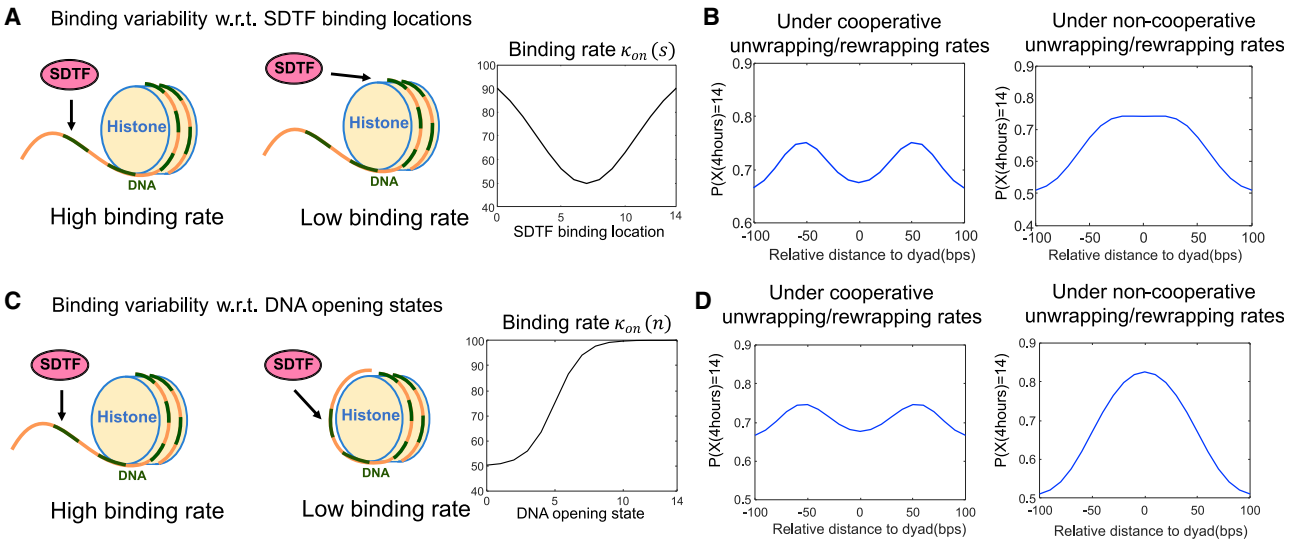

Figure 5. Consistency of the eviction probability profiles under more general parameter settings

(A) Generalization of the model where SDTF binding rate $\kappa_{on}(s)$ is a function of the binding location s.

(B) Resulting eviction probability profiles based on the binding rates illustrated in (A).

(C) Generalization of the model where the SDTF binding rate $\kappa_{on}(n)$ is a function of the DNA opening state n.

(D) Resulting eviction probability profiles based on the binding rates illustrated in (C).

See also Figure S6.

(Figures 4D and 4E). First, comparing the two systems, WT and Mut, allowed us to assess the distribution of stimulus-induced fold changes for each genomic location that are attributable to differences in signaling dynamics (Figure 4D). Second, the two experimental systems displayed differences in the amount of post-stimulation chromatin accessibility among genomic locations, which was recapitulated by the model (Figure 4E). We also computed the total variation distance, one of the most common measurements for similarity of given distributions (Levin and Peres, 2017), between the two experimentally measured distributions (STAR Methods) and found it to be 0.25. The distance between the two modeled distributions was 0.22, showing that modeled difference between the DNA accessibility under WT and Mut signals was similar to that from experiments. This comparison with experimental data helped validate the dynamic rates of DNA wrapping and unwrapping in the model.

Eviction probability profiles under more general parameter settings

We next found that the eviction probability profiles showed consistent shapes even under more biophysically nuanced SDTF binding parameters κ_{on}. We first allowed $\kappa_{on}(s)$ to vary as a function of the binding location s. We set $\kappa_{on}(s)$ to be smallest at the most inaccessible site, the nucleosome dyad (Figure 5A). Under such spatially inhomogeneous SDTF binding rates, the full eviction probability profile has the same characteristic shape as before; in the cooperative case, one can see two peaks, and in the non-cooperative case, there is only a single peak (Figure 5B). Second, we assumed that the SDTF binding rate $\kappa_{on}(n)$ depends on the state n of the nucleosome for a fixed SDTF binding location s. It is reasonable to assume that, when the SDTF binding location is exposed by DNA unwrapping, the SDTF has a higher binding rate than when the binding site is buried by wrapped DNA (Figure 5C). Under this general setting, the eviction probability profile robustly showed the characteristic shapes for he cooperative and non-cooperative cases (Figure 5D). The consistency of the model predictions to different parameter assumptions supports the robustness of the behaviors generated by our stochastic epigenome model as shown in Figure S6 and is mathematically verified in the STAR Methods.

Fitting the model to a different dataset results in consistent behavior

We hypothesized that the model parameters associated with nucleosome dynamics should be consistent in a second experiment with the same SDTF activated but by a different ligand. We thus stimulated wild-type macrophages with lipopolysaccharide (LPS) for 4 h to generate non-oscillatory NF-κB dynamics (Figure 6A), analogous to the non-oscillatory NF-κB dynamics generated by TNF stimulation in IκBα knockout mutant macrophages. We again performed paired-end ATAC-seq and identified the location of NF-κB binding sites relative to the nucleosome dyad (Figure 6B). Comparing nucleosome positions at 0 h and 4 h resulted in the experimental eviction probability profile, and the mathematical model was again fit to these data.

All experiments were performed in macrophages, but LPS stimulation may activate greater amounts of NF-κB than TNF. Hence, we first fit the model to the LPS-stimulated dataset with all of the same parameters obtained from the previous fit to TNF-simulated data but slightly adjusted SDTF unbinding fraction (*BF*) reflecting a greater amount of NF-κB. Remarkably, the model closely reproduced the eviction probability profile given by the LPS-stimulated dataset (Figure 6C). We next fit the eviction probability profile to the LPS-stimulated data using gradient descent, and the resulting

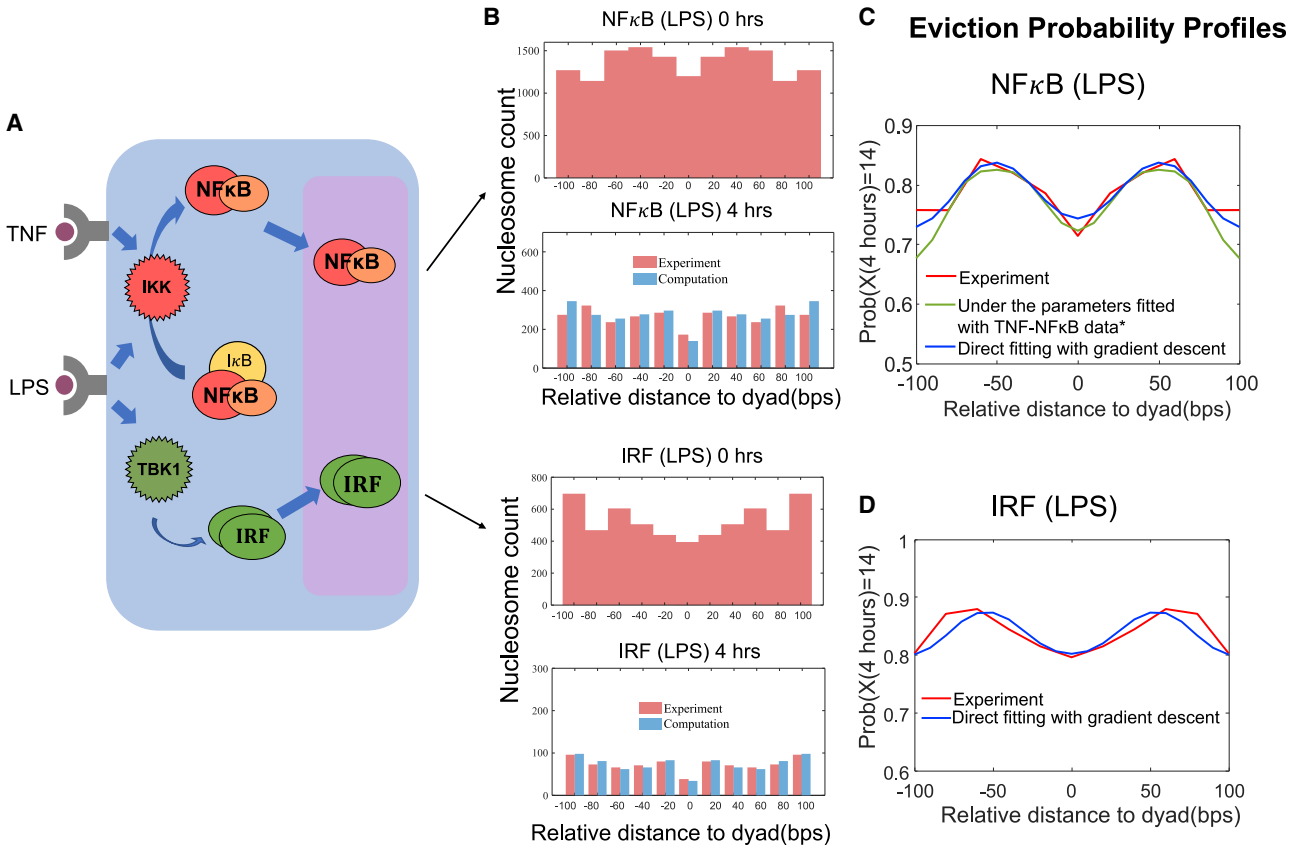

Figure 6. Stimulation of macrophages with LPS leads to consistent modeling results

(A) Schematic of SDTF activation in response to TNF or LPS. TNF stimulation results in NF-κB activity, whereas LPS stimulation results in NF-κB and IRF activity.

(B) Top: experimental and simulated nucleosome counts after LPS stimulation for NF-κB-associated nucleosome locations after 0 h and 4 h (no replicates used, n = 1 for each time point). Bottom: analogous counts for IRF-associated nucleosome locations (n = 1 for each time point).

(C) Eviction probability profiles associated with LPS-induced NF-κB activity, using the same model parameters as the TNF-induced data (green) and direct fit (blue). *All parameters are the same as the fitted parameters with the TNF data (Figure 4) except for the SDTF unbinding fraction, *BF*.

(D) Eviction probability profiles associated with LPS-induced IRF3 activity.

See also Figure S5.

parameters closely matched the parameters obtained from fitting to the TNF-stimulated dataset (Figure 6C; Table S1). We found a remarkable similarity in the estimated nucleosome unwrapping and rewrapping parameters as well as in the range of NF-κB effect. For example, the cooperativity constant is estimated at h = 1.4 with these new data, whereas it was measured at h = 1.35 with the previous TNF-stimulated data. This value is exponentiated to specify the unwrapping parameters at each step, and even at step 13, this difference gives a fold change in parameters of only $(1.4^{13} \times 0.15)/(1.35^{13} \times 0.16) = 1.48$.

The unwrapping/rewrapping parameters and the cooperativity may be specific to a set of nucleosomes, but the range of the SDTF effect may be SDTF specific. We therefore next asked to what extent the eviction probability profiles remained consistent under another SDTF. Interferon-regulatory factors (IRFs) are also activated by LPS (Figure 6A), affecting chromatin accessibility and enhancer formation at genomic positions containing IRF binding motifs (Cheng et al., 2021). We mapped the locations of IRF motifs in relation to the nucleosome dyads estimated from ATAC-seq data (Figure 6B), and we plotted the eviction probability profile by comparing nucleosomes before stimulation and 4 h thereafter. We again noted a double-peaked profile suggestive of cooperativity in nucleosome unwrapping/rewrapping parameters. To quantify this, we fit the stochastic model to the profile and obtained new parameter estimations for these IRF-affected epigenomic regions (Figure 6D; Table S1). A key difference between the parameters previously fit to NF-κB data was the unwrapping parameter $a_n = 0.07$, compared with $a_n = 0.15$ for the previous model. Because NF-κB and IRF bind to their motifs with distinct biophysical characteristics, stereochemistries, and to different locations of the genome, our results suggest that such differences also determine their nucleosome eviction characteristics.

The eviction probability profile is a fingerprint for kinetic features of nucleosome dynamics

We asked how different model parameters might affect the features of the eviction probability profile, and we found that

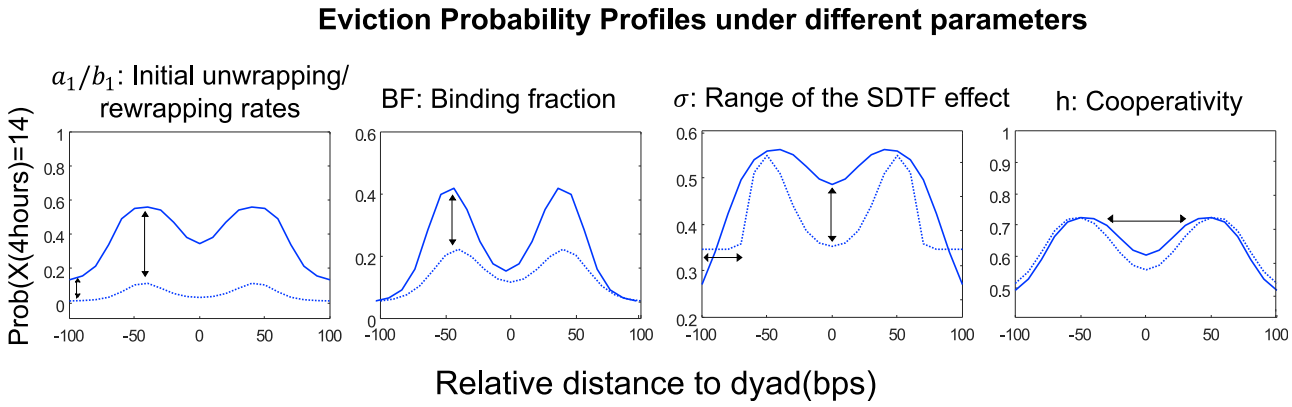

Figure 7. The eviction probability profile is a fingerprint for kinetic features of nucleosome dynamics

The geometric characteristics of the eviction probability profile has one-to-one correspondence to the parameters of the stochastic epigenome model. For a given location-specific nucleosome eviction profile, this correspondence can be used to identify epigenetic features such as the DNA unwrapping parameter, the SDTF binding fraction, and cooperativity.

See also Figure S5.

changes in model parameters could be directly mapped to changes in particular geometrical characteristics of the eviction probability profile (Figure 7). The unwrapping and rewrapping rates vertically translate the eviction probability profile because larger unwrapping parameters lead to larger eviction probabilities. Adjusting the SDTF unbinding fraction *BF* stretches the peaks up and down because the strength of the SDTF binding effect is determined by the SDTF binding fraction parameter (see STAR Methods and Figure S7 for a mathematical proof for this fact). More DNA-histone contact regions are influenced when the range of the SDTF binding effect is wide. Hence, the range parameter σ changes the depth of the center dip in the eviction probability profile. The other parameter, *BF*, controls the depth of the center dip as well, but a small σ particularly can create plateaus at both ends because the DNA around ± 100 relative bp is never affected by the SDTF binding when the effect range is narrow. The optimal SDTF binding location tends to shift toward the edges under strong cooperativity so that the distance between two peaks in the eviction probability profile increases as the cooperativity parameter *h* increases. Based on this one-to-one correspondence, we can systematically find a good initial prediction for the parameter fitting to given data, and this prediction can be used as an initial condition of the gradient descent searching algorithm for finer parameter fitting.

DISCUSSION

Our study pairs stochastic modeling and epigenomic chromatin accessibility measurements from primary cells to investigate the biophysical regulatory rules of histone octamer-DNA interactions that determine nucleosome positioning. Using probability theory, we described nucleosome eviction as a ''success or failure game'' scheme because DNA has a chance of full eviction only under the on-phase of the SDTF signal. This scheme revealed the role of oscillatory inputs in nucleosome eviction and heterogeneity in DNA accessibility under oscillatory SDTF dynamics. Nucleosome positioning data provided the nucleosome eviction probability profile as a function of SDTF motif location, and fitting model parameters to the eviction probability profile revealed quantitative features of nucleosome dynamics: (1) 30–40 bp of DNA-histone contacts around the SDTF binding site are disrupted, (2) the expected initial DNA unwrapping time from the fully wrapped state is about 7 min, and (3) evidence of cooperativity in the DNA unwrapping steps. Supportive of this model, these quantitative features of our model are consistent with previous experimental observations (Cheng et al., 2021).

Naturally, as with all mathematical models, the *in vivo* cellular system is more complex than the model describes, and our model is necessarily an abstraction describing one aspect of the dynamic epigenome that results when mammalian cells encounter an inflammatory threat. Nucleosome dynamics at each location along the genome are influenced by multiple factors, including, but not limited to, the stiffness of the local DNA, the histone marks or histone variants that are present, the density of nucleosomes at that region, and the binding motif location in relation to the position of the nucleosome (Brahma and Henikoff, 2020). However, our model is able to assess several characteristics of nucleosome dynamics that may govern the rules and parameter rates at which nucleosomes are evicted across the epigenome. These predictions help formulate hypotheses that are compared with time course epigenomic sequencing data, which allows selection of one of the hypotheses or establishment of parameter ranges.

Notably, the model can be used to evaluate numerous different stimulus-response systems, including those with different SDTFs activated (Calderon et al., 2019), or different cell types and genomic locations that may have different kinetic rates governing the unwrapping and rewrapping of the nucleosome. Here we focused on immune responses and the resulting epigenome of innate immune macrophages, but the modeling approach can be applied to other contexts as well where cells encounter an inflammatory signal that produces stimulus-induced epigenomic changes (for example, cancer cell plasticity during immunotherapy). For innate immune responses in

particular, the variation in the baseline epigenome that results from a prior exposure, rather than variation in genetically encoded receptors like for T and B cells, may be a critical component of innate immune memory and response to future inflammatory threats (Netea et al., 2016). Thus, a predictive mechanistic understanding of how SDTF activity can evict nucleosomes can guide further investigation into epigenomic reprogramming events induced by inflammation.

The development and parameterization of this mechanistic model has several implications. First, the model may allow predictions of nucleosome eviction probabilities in response to any SDTF and any activation dynamics. Second, because the relationship of the motif location and nucleosome dyad correlates with eviction probability, the model can make a prediction on the probability for nucleosome eviction in a location-specific manner. Third, the model arrives at biological insights related to the nucleosome parameters themselves; by comparing pre- and post-stimulation nucleosome distributions, we can calculate experimental nucleosome eviction probabilities and fit the model to estimate the degree of cooperativity within the nucleosome and the range of effect of SDTF binding on disrupting nucleosomal contact points.

This stochastic model describes the nucleosome, which is the fundamental unit of chromatin containing multi-step dynamic processes, and serves as a starting point for describing other epigenomic features (Bilokapic et al., 2018; Eslami-Mossallam et al., 2016; Hall et al., 2009; Henikoff, 2016). Future work incorporating other key elements of nucleosome dynamics, such as the structure of nucleosome arrays and the effect of histone modifications, or behaviors such as nucleosome sliding or rolling, which we have not yet considered here, may reveal further insights. Although here we use an optimization approach to analyze this model topology and initial conditions with respect to the data, model parameters can also be further trained with machine learning approaches that incorporate additional layers of epigenomic data as training data for the parameters to incorporate more elements of the epigenomic complexity that exists *in vivo*. Our modeling framework and these further possibilities support the feasibility of combining biophysically detailed mechanistic models of epigenetic processes, with NGS epigenome-wide measurements to characterize kinetic rules controlling cellular responses to inflammation.

Limitations of the study

Our stochastic model describes one process of how epigenomic states may be altered: through activation of SDTFs and the effect of their DNA binding in disrupting the positions of nucleosomes. Within cells, however, other proteins and enzymes also play key roles in how readily nucleosomes are evicted; for example, deposition of histone modifications, the presence of histone chaperones, or histone variants substituting for canonical histone subunits. The activity of these other processes likely varies across different cell types and different cell states; for example, in cancer cells versus immune cells versus epithelial cells. The models we present here, although biophysically detailed, still represent an abstraction of a more complex interplay among many chromatin remodeling proteins. In another system, an increase in the estimated cooperativity, or range of SDTF effect, may suggest not simply a direct biophysical change in the modeled components but could also indicate the activity of unmodeled proteins. Using mathematical models such as those described here to estimate such parameters across different experimental systems will suggest further hypotheses that motivate continual inclusion of additional mechanisms in future models.

STAR★METHODS

Detailed methods are provided in the online version of this paper and include the following:

- KEY RESOURCES TABLE
- RESOURCE AVAILABILITY
  - Lead contact
  - Materials availability
  - Data and code availability
- EXPERIMENTAL MODEL AND SUBJECT DETAILS
  - Macrophage cell culture
- METHOD DETAILS
  - ATAC sequencing
  - Stochastic model for nucleosome accessibility
- QUANTIFICATION AND STATISTICAL ANALYSIS
  - Model simulations
  - Coefficients variation
  - Total variation distance
  - ATAC-seq data processing
  - ATAC-seq nucleosome analysis

SUPPLEMENTAL INFORMATION

Supplemental information can be found online at https://doi.org/10.1016/j.celrep.2022.111076.

ACKNOWLEDGMENTS

J.K. and G.E. were partially supported by NSF grants DMS1763272 and DMS1616233 and Simons Foundation grant 594598 (Qing Nie). J.K. is supported by the Basic Science Research Institute Fund, whose NRF grant number is 2021R1A6A1A10042944. K.M.S. is supported by the UCLA Medical Scientist Training Program (NIH NIGMS T32-GM008042) and a Systems and Integrative Biology training grant (T32-GM008185). A.H. was funded by R01AI127864. We thank Sho Ohta for early access to the macrophage sequencing data and paired-end resequencing of the macrophage ATAC-seq libraries published in Cheng et al. (2021). Data sequencing for this paper was performed with the services of the UCLA Technology Center for Genomics and Bioinformatics Sequencing Core. We also thank the NSF-Simons Center for Multiscale Cell Fate for an Interdisciplinary Opportunity Award that initiated this project.

AUTHOR CONTRIBUTIONS

J.K., K.M.S., A.H., and G.E. conceived the project. J.K. and K.M.S. developed the model and analyzed the data. J.K. analyzed the model and performed model computations. K.M.S. performed bioinformatics analyses of the data. K.M.S. and Q.J.C. performed ATAC-seq experiments. J.K., K.M.S., A.H., and G.E. wrote the paper.

DECLARATION OF INTERESTS

The authors declare no competing interests.

Received: March 2, 2021
Revised: February 17, 2022
Accepted: June 20, 2022
Published: July 12, 2022

REFERENCES

Adelaja, A., Taylor, B., Sheu, K.M., Liu, Y., Luecke, S., and Hoffmann, A. (2021). Six distinct NFκB signaling codons convey discrete information to distinguish stimuli and enable appropriate macrophage responses. Immunity *54*, 916–930.e7. https://doi.org/10.1016/j.immuni.2021.04.011.

Alberts, B., Johnson, A., Lewis, J., Raff, M., Roberts, K., and Walter, P. (2002). Chromosomal DNA and its packaging in the chromatin fiber. Mol. Biol. Cell.

Allfrey, V.G., Littau, V.C., and Mirsky, A.E. (1963). On the role of histones in regulating ribonucleic acid synthesis in the cell nucleus. Proc. Natl. Acad. Sci. USA *49*, 414–421. https://doi.org/10.1073/pnas.49.3.414.

Ali Al-Radhawi, M., Del Vecchio, D., and Sontag, E.D. (2019). Multi-modality in gene regulatory networks with slow promoter kinetics. PLoS Comput. Biol. *15*, e1006784. https://doi.org/10.1371/journal.pcbi.1006784.

Barken, D., Wang, C.J., Kearns, J., Cheong, R., Hoffmann, A., and Levchenko, A. (2005). Comment on "oscillations in NF- B signalling control the dynamics of gene expression". Science *308*, 52a. https://doi.org/10.1126/science.1107904.

Bednar, J., Garcia-Saez, I., Boopathi, R., Cutter, A.R., Papai, G., Reymer, A., Syed, S.H., Lone, I.N., Tonchev, O., Crucifix, C., et al. (2017). Structure and dynamics of a 197 bp nucleosome in complex with linker histone H1. Mol. Cell *66*, 384–397.e8. https://doi.org/10.1016/j.molcel.2017.04.012.

Behar, M., and Hoffmann, A. (2010). Understanding the temporal codes of intra-cellular signals. Curr. Opin. Genet. Dev. *20*, 684–693. https://doi.org/10.1016/j.gde.2010.09.007.

Bilokapic, S., Strauss, M., and Halic, M. (2018). Histone octamer rearranges to adapt to DNA unwrapping. Nat. Struct. Mol. Biol. *25*, 101–108. https://doi.org/10.1038/s41594-017-0005-5.

Brahma, S., and Henikoff, S. (2020). Epigenome regulation by dynamic nucleosome unwrapping. Trends Biochem. Sci. *45*, 13–26. https://doi.org/10.1016/j.tibs.2019.09.003.

Courant, Richard (1994). Variational methods for the solution of problems of equilibrium and vibrations. Lecture notes in pure and applied mathematics, 1.

de Bruin, L., Tompitak, M., Eslami-Mossallam, B., and Schiessel, H. (2016). Why do nucleosomes unwrap asymmetrically? J. Phys. Chem. B *120*, 5855–5863. https://doi.org/10.1021/acs.jpcb.6b00391.

Buenrostro, J.D., Wu, B., Chang, H.Y., and Greenleaf, W.J. (2015). ATAC-seq: a method for assaying chromatin accessibility genome-wide. Curr. Protoc. Mol. Biol. *109*, 1–21. https://doi.org/10.1002/0471142727.mb2129s109.

Calderon, D., Nguyen, M.L.T., Mezger, A., Kathiria, A., Müller, F., Nguyen, V., Lescano, N., Wu, B., Trombetta, J., Ribado, J.V., et al. (2019). Landscape of stimulation-responsive chromatin across diverse human immune cells. Nat. Genet. *51*, 1494–1505. https://doi.org/10.1038/s41588-019-0505-9.

Callegari, A., Sieben, C., Benke, A., Suter, D.M., Fierz, B., Mazza, D., and Manley, S. (2019). Single-molecule dynamics and genome-wide transcriptomics reveal that NF-kB (p65)-DNA binding times can be decoupled from transcriptional activation. PLoS Genet. *15*, e1007891. https://doi.org/10.1371/journal.pgen.1007891.

Chen, P., Dong, L., Hu, M., Wang, Y.-Z., Xiao, X., Zhao, Z., Yan, J., Wang, P.-Y., Reinberg, D., Li, M., et al. (2018). Functions of FACT in breaking the nucleosome and maintaining its integrity at the single-nucleosome level. Mol. Cell *71*, 284–293.e4. https://doi.org/10.1016/j.molcel.2018.06.020.

Cheng, Q.J., Ohta, S., Sheu, K.M., Spreafico, R., Adelaja, A., Taylor, B., and Hoffmann, A. (2021). NF-κB dynamics determine the stimulus specificity of epigenomic reprogramming in macrophages. Science *372*, 1349–1353. https://doi.org/10.1126/science.abc0269.

Chou, T. (2007). Peeling and sliding in nucleosome repositioning. Phys. Rev. Lett. *99*, 058105. https://doi.org/10.1103/PhysRevLett.99.058105.

Dechassa, M.L., Sabri, A., Pondugula, S., Kassabov, S.R., Chatterjee, N., Kladde, M.P., and Bartholomew, B. (2010). SWI/SNF has intrinsic nucleosome disassembly activity that is dependent on adjacent nucleosomes. Mol. Cell *38*, 590–602. https://doi.org/10.1016/j.molcel.2010.02.040.

Dobrovolskaia, I.V., and Arya, G. (2012). Dynamics of forced nucleosome unraveling and role of nonuniform histone-DNA interactions. Biophys. J. *103*, 989–998. https://doi.org/10.1016/j.bpj.2012.07.043.

Dodd, I.B., Micheelsen, M.A., Sneppen, K., and Thon, G. (2007). Theoretical analysis of epigenetic cell memory by nucleosome modification. Cell *129*, 813–822. https://doi.org/10.1016/j.cell.2007.02.053.

Eslami-Mossallam, B., Schiessel, H., and van Noort, J. (2016). Nucleosome dynamics: sequence matters. Adv. Colloid Interface Sci. *232*, 101–113. https://doi.org/10.1016/j.cis.2016.01.007.

Hall, M.A., Shundrovsky, A., Bai, L., Fulbright, R.M., Lis, J.T., and Wang, M.D. (2009). High resolution dynamic mapping of histone-DNA interactions in a nucleosome. Nat. Struct. Mol. Biol. *16*, 124–129. https://doi.org/10.1038/nsmb.1526.

Heinz, S., Benner, C., Spann, N., Bertolino, E., Lin, Y.C., Laslo, P., Cheng, J.X., Murre, C., Singh, H., and Glass, C.K. (2010). Simple combinations of lineage-determining transcription factors prime cis-regulatory elements required for macrophage and B cell identities. Mol. Cell *38*, 576–589. https://doi.org/10.1016/j.molcel.2010.05.004.

Henikoff, S. (2016). Mechanisms of nucleosome dynamics in vivo. Cold Spring Harb. Perspect. Med. *6*, a026666. https://doi.org/10.1101/cshperspect.a026666.

Hoffmann, A., Levchenko, A., Scott, M.L., and Baltimore, D. (2002). The IκB-NF-κb signaling module: temporal control and selective gene activation. Science *298*, 1241–1245. https://doi.org/10.1126/science.1071914.

Kim, J., and Enciso, G. (2020). Absolutely robust controllers for chemical reaction networks. J. R. Soc. Interface *17*, 20200031. https://doi.org/10.1098/rsif.2020.0031.

Klemm, S.L., Shipony, Z., and Greenleaf, W.J. (2019). Chromatin accessibility and the regulatory epigenome. Nat. Rev. Genet. *20*, 207–220. https://doi.org/10.1038/s41576-018-0089-8.

Konrad, S.F., Vanderlinden, W., Frederickx, W., Brouns, T., Menze, B.H., De Feyter, S., and Lipfert, J. (2021). High-throughput AFM analysis reveals unwrapping pathways of H3 and CENP-A nucleosomes. Nanoscale *13*, 5435–5447. https://doi.org/10.1039/D0NR08564B.

Kurtz, T.G. (1980). Representations of Markov processes as multiparameter time changes. Ann. Probab. *8*, 682–715. https://doi.org/10.1214/aop/1176994660.

Lee, C.-K., Shibata, Y., Rao, B., Strahl, B.D., and Lieb, J.D. (2004). Evidence for nucleosome depletion at active regulatory regions genome-wide. Nat. Genet. *36*, 900–905. https://doi.org/10.1038/ng1400.

Lee, R.E., Walker, S.R., Savery, K., Frank, D.A., and Gaudet, S. (2014). fold change of nuclear NF-κB determines TNF-induced transcription in single cells. Mol. Cell *53*, 867–879. https://doi.org/10.1016/j.molcel.2014.01.026.

Levin, David A., and Peres, Yuval (2017). Markov chains and mixing times.*107* (American Mathematical Soc).

Li, G., Levitus, M., Bustamante, C., and Widom, J. (2005). Rapid spontaneous accessibility of nucleosomal DNA. Nat. Struct. Mol. Biol. *12*, 46–53. https://doi.org/10.1038/nsmb869.

Liu, Y., Zhou, K., Zhang, N., Wei, H., Tan, Y.Z., Zhang, Z., Carragher, B., Potter, C.S., D'Arcy, S., and Luger, K. (2020). FACT caught in the act of manipulating the nucleosome. Nature *577*, 426–431. https://doi.org/10.1038/s41586-019-1820-0.

Longo, D.M., Selimkhanov, J., Kearns, J.D., Hasty, J., Hoffmann, A., and Tsimring, L.S. (2013). Dual delayed feedback provides sensitivity and robustness to the NF-κB signaling module. PLoS Comput. Biol. *9*, e1003112. https://doi.org/10.1371/journal.pcbi.1003112.

Luger, K., Mäder, A.W., Richmond, R.K., Sargent, D.F., and Richmond, T.J. (1997). Crystal structure of the nucleosome core particle at 2.8 Å resolution. Nature *389*, 251–260. https://doi.org/10.1038/38444.

Luger, K., Dechassa, M.L., and Tremethick, D.J. (2012). New insights into nucleosome and chromatin structure: an ordered state or a disordered affair? Nat. Rev. Mol. Cell Biol. *13*, 436–447. https://doi.org/10.1038/nrm3382.

Mauney, A.W., Tokuda, J.M., Gloss, L.M., Gonzalez, O., and Pollack, L. (2018). Local DNA sequence controls asymmetry of DNA unwrapping from nucleosome core particles. Biophys. J. *115*, 773–781. https://doi.org/10.1016/j.bpj.2018.07.009.

Méléard, S., and Villemonais, D. (2012). Quasi-stationary distributions and population processes. Probability Surveys *9*, 340–410. https://doi.org/10.1214/11-PS191.

Miller, J.A., and Widom, J. (2003). Collaborative competition mechanism for gene activation *in vivo*. Mol. Cell Biol. *23*, 1623–1632. https://doi.org/10.1128/MCB.23.5.1623-1632.2003.

Möbius, W., Neher, R.A., and Gerland, U. (2006). Kinetic accessibility of buried DNA sites in nucleosomes. Phys. Rev. Lett. *97*, 208102. https://doi.org/10.1103/PhysRevLett.97.208102.

Möbius, W., Osberg, B., Tsankov, A.M., Rando, O.J., and Gerland, U. (2013). Toward a unified physical model of nucleosome patterns flanking transcription start sites. Proc. Natl. Acad. Sci. USA *110*, 5719–5724. https://doi.org/10.1073/pnas.1214048110.

Netea, M.G., Joosten, L.A.B., Latz, E., Mills, K.H.G., Natoli, G., Stunnenberg, H.G., ONeill, L.A.J., and Xavier, R.J. (2016). Trained immunity: a program of innate immune memory in health and disease. Science *352*, aaf1098. https://doi.org/10.1126/science.aaf1098.

Ngo, T.T.M., Zhang, Q., Zhou, R., Yodh, J.G., and Ha, T. (2015). Asymmetric unwrapping of nucleosomes under tension directed by DNA local Flexibility. Cell *160*, 1135–1144. https://doi.org/10.1016/j.cell.2015.02.001.

Ostuni, R., Piccolo, V., Barozzi, I., Polletti, S., Termanini, A., Bonifacio, S., Curina, A., Prosperini, E., Ghisletti, S., and Natoli, G. (2013). Latent enhancers activated by stimulation in differentiated cells. Cell *152*, 157–171. https://doi.org/10.1016/j.cell.2012.12.018.

Polach, K.J., and Widom, J. (1995). Mechanism of protein access to specific DNA sequences in chromatin: a dynamic equilibrium model for gene regulation. J. Mol. Biol. *254*, 130–149. https://doi.org/10.1006/jmbi.1995.0606.

Purvis, J.E., and Lahav, G. (2013). Encoding and decoding cellular information through signaling dynamics. Cell *152*, 945–956. https://doi.org/10.1016/j.cell.2013.02.005.

Quinlan, A.R., and Hall, I.M. (2010). BEDTools: a flexible suite of utilities for comparing genomic features. Bioinformatics *26*, 841–842. https://doi.org/10.1093/bioinformatics/btq033.

Schep, A.N., Buenrostro, J.D., Denny, S.K., Schwartz, K., Sherlock, G., and Greenleaf, W.J. (2015). Structured nucleosome fingerprints enable high-resolution mapping of chromatin architecture within regulatory regions. Genome Res. *25*, 1757–1770. https://doi.org/10.1101/gr.192294.115.

Segal, E., and Widom, J. (2009). What controls nucleosome positions? Trends Genet. *25*, 335–343. https://doi.org/10.1016/j.tig.2009.06.002.

Segal, E., Fondufe-Mittendorf, Y., Chen, L., Thåström, A., Field, Y., Moore, I.K., Wang, J.-P.Z., and Widom, J. (2006). A genomic code for nucleosome positioning. Nature *442*, 772–778. https://doi.org/10.1038/nature04979.

Sen, S., Cheng, Z., Sheu, K.M., Chen, Y.H., and Hoffmann, A. (2020). Gene regulatory strategies that decode the duration of NFκB dynamics contribute to LPS- versus TNF-specific gene expression. Cell Syst. *10*, 169–182.e5. https://doi.org/10.1016/j.cels.2019.12.004.

Shinar, G., and Feinberg, M. (2010). Structural sources of robustness in biochemical reaction networks. Science *327*, 1389–1391. https://doi.org/10.1126/science.1183372.

Shivaswamy, S., Bhinge, A., Zhao, Y., Jones, S., Hirst, M., and Iyer, V.R. (2008). Dynamic remodeling of individual nucleosomes across a eukaryotic genome in response to transcriptional perturbation. PLoS Biol. *6*, e65. https://doi.org/10.1371/journal.pbio.0060065.

Shoval, O., Goentoro, L., Hart, Y., Mayo, A., Sontag, E., and Alon, U. (2010). Fold-change detection and scalar symmetry of sensory input fields. Proc. Natl. Acad. Sci. USA *107*, 15995–16000. https://doi.org/10.1073/pnas.1002352107.

Singh, A., Sen, S., Adelaja, A., and Hoffmann, A. (2022). Stimulus-Response signaling dynamics characterize macrophage polarization states. Preprint at bioRxiv. https://doi.org/10.1101/2022.03.27.485991.

Stelling, J., Gilles, E.D., and Doyle, F.J. (2004). Robustness properties of circadian clock architectures. Proc. Natl. Acad. Sci. USA *101*, 13210–13215. https://doi.org/10.1073/pnas.0401463101.

Stewart, A.J., Hannenhalli, S., and Plotkin, J.B. (2012). Why transcription factor binding sites are ten nucleotides long. Genetics *192*, 973–985. https://doi.org/10.1534/genetics.112.143370.

Tims, H.S., Gurunathan, K., Levitus, M., and Widom, J. (2011). Dynamics of nucleosome invasion by DNA binding proteins. J. Mol. Biol. *411*, 430–448. https://doi.org/10.1016/j.jmb.2011.05.044.

Voliotis, Margaritis, Thomas, Philipp, Grima, Ramon, and Bowsher, Clive G (2016). Stochastic simulation of biomolecular networks in dynamic environments. PLoS computational biology *12*, 6. https://doi.org/10.1371/journal.pcbi.1004923.

Weinmann, A.S., Plevy, S.E., and Smale, S.T. (1999). Rapid and selective remodeling of a positioned nucleosome during the induction of IL-12 p40 transcription. Immunity *11*, 665–675. https://doi.org/10.1016/S1074-7613(00)80141-7.

Werner, S.L., Barken, D., and Hoffmann, A. (2005). Stimulus specificity of gene expression programs determined by temporal control of IKK activity. Science *309*, 1857–1861. https://doi.org/10.1126/science.1113319.

Zhou, K., Gaullier, G., and Luger, K. (2019). Nucleosome structure and dynamics are coming of age. Nat. Struct. Mol. Biol. *26*, 3–13. https://doi.org/10.1038/s41594-018-0166-x.

STAR★METHODS

KEY RESOURCES TABLE

REAGENT or RESOURCE	SOURCE	IDENTIFIER
Chemicals, peptides, and recombinant proteins		
LPS	Sigma, B5:055	L2880
murine TNF	Roche	11271156001
Experimental models: Cell lines		
Immortalized Myeloid Progenitor-derived macrophages	Singh et al., 2022	N/A
Experimental models: Organisms/strains		
C57Bl/6 mouse *Nfkbia*$^{-/-}$ *Rel*$^{-/-}$ *Tnf*$^{-/-}$ *Nfkbie*$^{-/-}$ BMDMs	Cheng et al., 2021	N/A
Deposited data		
Macrophage PE ATACseq	This paper	GSE156385
Macrophage SE ATACseq	Cheng et al., 2021	GSE146068
Software and algorithms		
MATLAB 2016b		https://matlab.mathworks.com/
R (version 4.0.3)		https://www.r-project.org/
ENCODE-DCC ATACseq Pipeline		https://github.com/ENCODE-DCC/atac-seq-pipeline
Bedtools	Quinlan and Hall, 2010	https://bedtools.readthedocs.io/en/latest/
NucleoATAC	Schep et al., 2015	https://github.com/GreenleafLab/NucleoATAC
HOMER	Heinz et al., 2010	http://homer.ucsd.edu/homer/ngs/peakMotifs.html
Nucleosome Model Code	This paper	https://10.5281/zenodo.6503369 (https://github.com/signalingsystemslab/nucleosome_stochasticModel)

RESOURCE AVAILABILITY

Lead contact

Further information and requests for resources and materials should be directed to and will be fulfilled by the Lead Contact, German Enciso (enciso@uci.edu).

Materials availability

No materials were generated in this paper.

Data and code availability

ATAC-seq data have been deposited at GEO and are publicly available as of the date of publication. Accession numbers are listed in the Key resources table.

This paper analyzes existing, publicly available data. These accession numbers for the datasets are listed in the Key resources table.

Model and analysis code includes MATLAB code for running the stochastic model, and bioinformatic analysis of sequencing data. All original code has been deposited to Github and is publicly available as of the date of publication. DOIs are listed in the Key resources table.

Any additional information required to reanalyze the data reported in this paper is available from the lead contact upon request.

EXPERIMENTAL MODEL AND SUBJECT DETAILS

Macrophage cell culture

All mouse experiments were approved by the UCLA animal research committee under protocols ARC2014-110 and ARC-2014-126. Macrophages were obtained via two methods: (1) differentiating bone-marrow-derived monocytes from male C57BL/6 mice in DMEM/10% FBS +30% L929 supernatant for a total of 7 days, or (2) differentiating immortalized myeloid progenitors (iMPs) originally derived from male C57BL/6 mice, in DMEM/10% FBS +30% L929 supernatant for a total of 10 days. BMDM data was obtained from

paired-end resequencing of the same libraries that had been sequenced single-ended in Cheng et al. (2021), so no additional mice were used for this paper. As described in Cheng et al. (2021), sex-matched bone marrow-derived macrophages (BMDMs) were prepared by culturing bone marrow monocytes from femurs of 8-12-week-old mice in DMEM/10% FBS +30% L929 supernatant medium using standard methods (Cheng et al., 2021; Adelaja et al., 2021). BMDMs were re-plated in experimental dishes on day 4, and stimulated on day 7 with 10ng/mL murine TNF (Roche 11271156001) for 4 h. For iMP-derived macrophages (iMPDMs), cells were replated into 6cm plates with new media on day 7, at a density of ~20k cells/cm^2. On day 10, cells were stimulated 100ng/mL lipopolysaccharide (LPS, Sigma Aldrich) for 4 h.

METHOD DETAILS

ATAC sequencing

Control and stimulated immortalized myeloid progenitor derived macrophages (iMPDMs) were dissociated with Accutase (Thermo Fisher Scientific), and 50,000 cells were used per sample. Cell membranes were lysed using cold lysis buffer (10mM Tris-HCl pH7.5, 32 3mM MgCl2, 10mM NaCl and 0.1% IGEPAL CA-630). Nuclei were pelleted by centrifugation for 10 min at 500 x g and suspended in transposase reaction mixture (25 μL of 2X TD Buffer (Illumina), 2.5 μL of TD Enzyme 1 (Illumina), and 22.5 μL of nuclease-free water), and the transposase reaction was performed for 30 min at 37C in a thermomixer shaker. DNA was purified using MinElute PCR purification kit (QIAGEN, Hilden, Germany). Libraries were prepared for sequencing using Nextera DNA Library Preparation Kit (Illumina, FC-121). The libraries were purified using MinElute PCR purification kit (QIAGEN) and quantified using KAPA Library Quantification Kit (KAPA Biosystems). Libraries were sequenced paired end 2 × 100 on Illumina Novaseq.

Stochastic model for nucleosome accessibility

Stochastic modeling

Chromatin accessibility under a signal dependent transcription factor (SDTF) signal can be modeled as a non homogeneous time Markov process.

$$\begin{array}{ccccccccccc} (0,0) & \underset{a_1}{\overset{b_1}{\rightleftarrows}} & (1,0) & \underset{b_2}{\overset{a_2}{\rightleftarrows}} \cdots \underset{b_r}{\overset{a_r}{\rightleftarrows}} & (r,0) & \underset{b_{r+1}}{\overset{a_{r+1}}{\rightleftarrows}} \cdots \underset{b_{13}}{\overset{a_{13}}{\rightleftarrows}} & (13,0) & \xrightarrow{a_{14}} & (14,0) \\ k_{on}\downarrow\uparrow k_{off} & & k_{on}\downarrow\uparrow k_{off} & & k_{on}\downarrow\uparrow k_{off} & & k_{on}\downarrow\uparrow k_{off} & & k_{on}\downarrow\uparrow k_{off} \\ (0,1) & \underset{d_1}{\overset{c_1}{\rightleftarrows}} & (1,1) & \underset{d_2}{\overset{c_2}{\rightleftarrows}} \cdots \underset{d_r}{\overset{c_r}{\rightleftarrows}} & (r,1) & \underset{d_{r+1}}{\overset{c_{r+1}}{\rightleftarrows}} \cdots \underset{d_{13}}{\overset{c_{13}}{\rightleftarrows}} & (13,1) & \xrightarrow{c_{14}} & (14,1) \end{array} \quad \text{(Equation 1)}$$

where $\kappa_{on} = \kappa_{on}(t)$ is a function of time, which is proportional to the concentration of the SDTF at time t.

Let $(X(t), N(t))$ be a 2-dimensional Markov process defined on the state spaces shown in (Equation 1). $X(t) \in \{0, 1, \ldots, 14\}$ models the chromatin accessibility as state 14 represents the fully unwrapped nucleosome, while state 0 represents the fully wrapped nucleosome. The status of SDTF is modeled with $N(t) \in \{0, 1\}$ as $N(t) = 1$ means an SDTF binds to DNA, and otherwise $N(t) = 0$ means that no SDTF is bound to DNA at time t. We enumerate the state space as

$$\{(0,0), (1,0), \ldots, (14,0), (0,1), \ldots, (14,1)\},$$

so that for $i \in \{1, 2 \ldots, 15\}$ the i th state is $(i - 1, 0)$ and $i + 15$ th state is $(i - 1, 1)$. The infinitesimal probability change is described as for $n \in \{1, 2, \ldots, 14\}$,

$$P(X(t + \Delta t) = n | X(t) = n - 1, N(t) = 0) = a_n,$$

$$P(X(t + \Delta t) = n | X(t) = n - 1, N(t) = 1) = c_n, \quad \text{and}$$

for $n \in \{0, 1, \ldots, 13\}$,

$$P(X(t + \Delta t) = n - 1 | X(t) = n, N(t) = 0) = b_n$$

$$P(X(t + \Delta t) = n - 1 | X(t) = n, N(t) = 1) = d_n.$$

Probability density function, average, and the full eviction probability. Let $f(t)$ be the SDTF dynamics. Suppose that the SDTF binding rate $\kappa_{on}(t) = cf(t)$ for some constant $c > 0$. We first assume that $\kappa_{on}(t) \equiv \kappa_{on}$ is a constant function. Let Q be the transition rate matrix of the process $(X(t), N(t))$. Let states $\mathbf{n}$ and $\mathbf{m}$ be such that $\mathbf{n} = (n_1, n_2)$ and $\mathbf{m} = (m_1, m_2)$ where the first entry is the state of X and the second entry is the state of N. Then

$$Q_{\mathbf{nm}}(t) = \begin{cases} a_{n_1} & \text{when } n_1+1=m_1 \text{ and } n_2=m_2, \\ b_{n_1} & \text{when } n_1-1=m_1 \text{ and } n_2=m_2=0 \text{ for } n_1<14, \\ d_{n_1} & \text{when } n_1-1=m_1 \text{ and } n_2=m_2=1, \\ \kappa_{\text{on}} & \text{when } n_1=m_1, n_2=0 \text{ and } m_2=1, \\ \kappa_{\text{off}} & \text{when } n_1=m_1, n_2=1 \text{ and } m_2=0, \\ -\sum_{\mathbf{k}\neq\mathbf{n}} Q_{\mathbf{n},\mathbf{k}} & \text{when } \mathbf{n}=\mathbf{m}, \\ 0 & \text{otherwise.} \end{cases} \quad \text{(Equation 2)}$$

Then the joint probability density $p(t)$ of $(X(t), N(t))$ satisfies the master equation

$$\frac{d}{dt}p(t) = p(t)Q, \quad \text{(Equation 3)}$$

regarding $p(t)$ as a row vector. Hence $p(t) = \mu e^{Qt}$ where μ is the initial distribution, and e^{Qt} is the matrix exponential defined as $e^{Qt} = \sum_{n=0}^{\infty} \frac{Q^n t^n}{n!}$. Let U be the matrix each column of which is a right eigenvector of Q and let D be the diagonal matrix such that $D_{ii} = -\lambda_i$ where $-\lambda_i$ is the i th eigenvalue of Q. By Perron-Frobenius theorem, $-1 \leq -\lambda_k \leq 0$ for each k. Then Q is diagonalized as $Q = UDU^{-1}$. Then

$$p(t) = Ue^{Dt}U^{-1} = U\mathrm{diag}\left(e^{-\lambda_1 t}, e^{-\lambda_2 t}, \ldots, e^{-\lambda_{30} t}\right)U^{-1}.$$

We assume that $\mu = (1, 0, \ldots, 0)$ as the process is supposed to start at $(X(0), N(0)) = (0, 0)$. Then for a state i, the probability density $p(i, t)$ can be represented as

$$p(i,t) = \sum_k U_{1k} U_{ki}^{-1} e^{-\lambda_k t} \quad \text{(Equation 4)}$$

If $\kappa_{\text{on}}(t)$ is a binary oscillation function with the half-period T such as

$$\kappa_{\text{on}}(t) = \begin{cases} \kappa_{\text{on}} & \text{if } t \in [2nT, (2n+1)T) \text{ for some } n \\ 0 & \text{if } t \in [(2n+1)T, (2n+2)T) \text{ for some } n, \end{cases}$$

then the transition matrix Q can be defined differently on each period. Let Q_{on} and Q_{off} be the transition matrix corresponding to the interval $[2nT, (2n+1)T)$ and $[(2n+1)T, (2n+2)T)$, respectively. Then for $t \in [2nT, (2n+1)T)$, the probability density function $p(t)$ is given as

$$p(t) = \mu e^{Q_{\text{on}}T} e^{Q_{\text{off}}T} \cdots e^{Q_{\text{on}}T} e^{Q_{\text{off}}T} e^{Q_{\text{on}}(t-2nT)} = \mu \left(e^{Q_{\text{on}}T} e^{Q_{\text{off}}T}\right)^n e^{Q_{\text{on}}(t-2nT)}. \quad \text{(Equation 5)}$$

If $t \in [(2n+1)T, (2n+2)T)$, then

$$p(t) = \mu e^{Q_{\text{on}}T} e^{Q_{\text{off}}T} \cdots e^{Q_{\text{on}}T} e^{Q_{\text{off}}(t-(2n+1)T)} = \mu \left(e^{Q_{\text{on}}T} e^{Q_{\text{off}}T}\right)^n e^{Q_{\text{on}}T} e^{Q_{\text{off}}(t-(2n+1)T)}. \quad \text{(Equation 6)}$$

Hence the full eviction probability by time T is $P(X(T) = 14) = p(15, T) + p(30, T)$, and the mean accessibility at time T is $\sum_{i=1}^{15}(i-1)(p(i,T) + p(i+15,T))$.

To incorporate the effect of SDTF binding, we set the rewrapping parameter with SDTF binding as $d_n = b_n\left(1 - exp\left(-\frac{(n-s)^2}{2\sigma^2}\right)\right)$, where s is the position of the binding motif and σ represents the range of SDTF effect. This similarity between the structure of the stochastic model and what can be measured in biological experiments allowed us to evaluate theoretical predictions using genomic sequencing data of *in vivo* cellular immune response systems.

Since $X(t)$ represents the accessibility state at any time t, the mean nucleosome accessibility can be computed as $\sum_{n=0}^{14} n Prob(X(t) = n)$. Also, since full eviction is reached at state 14, we could compute the probability of eviction by time T by calculating Prob $(X(T) = 14)$.

Model reduction. In this section, we show that the behavior of the SDTF binding, $N(t)$, in the stochastic model (1) is almost determined by $BF = \frac{\kappa_{\text{off}}}{\kappa_{\text{on}} + \kappa_{\text{off}}}$ provided that κ_{on} and κ_{off} are much bigger than a_n and b_n. We assume that $\kappa_{\text{on}}(t) \equiv \kappa_{\text{on}}$ for some positive constant κ_{on} and show that our model can be approximated with a simplified system, which only depends on a_n, b_n, d_n and the ratio BF. With this approximation, we conclude that the original system (1) depends on the ratio BF, not individual values of κ_{on} and κ_{off}.

Because of the separation of the timescales, the probability of $N(t)$ is stabilized quickly at a stationary distribution π_N such that $\pi_N(0) = \frac{\kappa_{\text{off}}}{\kappa_{\text{on}} + \kappa_{\text{off}}}$ and $\pi_N(1) = \frac{\kappa_{\text{on}}}{\kappa_{\text{off}} + \kappa_{\text{on}}}$. Therefore we can reduce the model assuming that the state of $N(t)$ is determined with the probability rule π_N. Then the transition probability $P(X(t+\Delta t) = i-1 | X(t) = i)$ for $X(t)$ can be simply calculated. We prove this rigorously by using quasi-stationary distribution of the coupled process (X, N).

For a small scaling parameter $0 < \epsilon < 1$, we scale the DNA unwrapping and rewrapping rates as $a_n^\epsilon = \epsilon a_n$, $b_n^\epsilon = \epsilon b_n$ and $d_n^\epsilon = \epsilon d_n$, where a_n, b_n and d_n are constant in ϵ. We also assume that κ_{on} and κ_{off} are constant in ϵ. Under this parameter scaling, to approximate the transition probabilities, we first note that

$$\begin{aligned}
&P(X(t+\Delta t)=n-1|X(t)=n)\\
&=P(X(t)=n-1|X(t)=n,N(t)=0)P(N(t)=0|X(t)=i)\\
&+P(X(t)=n-1|X(t)=n,N(t)=1)P(N(t)=1|X(t)=i)\\
&=b_n^{\epsilon}\Delta tP(N(t)=0|X(t)=n)+d_n^{\epsilon}\Delta tP(N(t)=1|X(t)=i)\\
&=b_n^{\epsilon}\Delta t\frac{P((X(t),N(t))=(n,0))}{P(X(t)=n)}+d_n^{\epsilon}\Delta t\frac{P((X(t),N(t))=(n,1))}{P(X(t)=n)}
\end{aligned} \tag{Equation 7}$$

for $n\in\{0,1,2,\ldots,13\}$. As (4) indicates, the probability vector $p(t)$ is expressed with eigenvalues of Q. By using this fact, we show that the probabilities

$$\frac{P((X(t),N(t))=(n,0))}{P(X(t)=n)}\quad\text{and}\quad\frac{P((X(t),N(t))=(n,1))}{P(X(t)=n)}$$

are approximately BF and $1-BF$, respectively. We first investigate the eigenvalues of Q with respect to ϵ.

Lemma 1.1 *Each eigenvalue* $-\lambda_k$ *of the transition rate matrix* Q *in* (Equation 2) *is either* $O(1)$ *or* $O(\epsilon)$.

Proof. Let $-\lambda_k$ be the eigenvalues of Q. By definition of the transition rate matrix Q (2), the trace of Q is $\alpha\epsilon+\beta$ for some constants α and β. Since the trace of a matrix is the sum of all eigenvalues, we have

$$-\sum_k\lambda_k=-\sum_{\lambda_k=O(1)}\lambda_k-\sum_{\lambda_k\neq O(1)}\lambda_k=\alpha\epsilon+\beta.$$

This implies that $-\sum_{\lambda_k\neq O(1)}\lambda_k=\alpha\epsilon$. Since $\lambda_k\geq 0$, the result follows.

We denote $-\lambda_k$ in $O(\epsilon)$ by $-\lambda_k(\epsilon)$. We assume that λ_i is in $O(\epsilon)$ for $i=1,2,\ldots,m$ for some m. By Lemma 1.1 and (4), the probability vector $p(t)$ can be decomposed as

$$p(t)=\pi+\sum_{k=1}^{m}q_k\eta^k e^{-\lambda_k(\epsilon)t}+\sum_{j=m+1}^{29}u_j\zeta^j e^{-\lambda_k t}, \tag{Equation 8}$$

where η^k and ζ^j are the left eigenvectors of Q, q_k and u_j are some constants, and π is a stationary distribution of (X,N). Note that since the process (X,N) eventually absorbs at the 15 th and 30 th states (i.e. states $(14,0)$ and $(14,1)$), it follows that $\pi(\mathbf{n})=0$ for each $\mathbf{n}=(n_1,n_2)$ such that $n_1\leq 13$. Thus to approximate $P(X(t)=n_1)$ and $P(N(t)=n_2)$ for each (n_1,n_2) such that $n_1\leq 13$, we need to calculate the entries of η_k, which are dominating term in (Equation 8).

To do that, we use a singular perturbation method. In (Al-Radhawi et al., 2019), this approach was employed to study asymptotic of the stationary distribution of stochastic systems admitting multi-modes. Let $Q=Q_1+\epsilon Q_2$ where Q_1 and Q_2 correspond to the transitions of N and the transitions of X, respectively. In the following lemma, we approximate the left eigenvector associated with $\lambda_k(\epsilon)$ by using a singular perturbation method.

Lemma 1.2 *For each left eigenvector* η^k *of* Q *associated with* $\lambda_k(\epsilon)$*, we have*

$$\lim_{\epsilon\to 0}\frac{\eta^k(i+15)}{\eta^k(i)}=\frac{\kappa_{on}}{\kappa_{off}}\quad\text{as long as }\ \eta^k(i)=O(1)\ \text{ for }\ i=1,2,\ldots,13. \tag{Equation 9}$$

Furthermore there exists a η^k such that $\eta_i^k=O(1)$ for each i.

Proof. For each $k=1,2,\ldots,m$, we define $\eta^k=\overline{\eta}^k+\epsilon\tilde{\eta}^k+h^k(\epsilon)$ where $\overline{\eta}^k$ and $\tilde{\eta}^k$ are constant in ϵ and $h^k(\epsilon)$ represents the higher order term. Then we have

$$\lambda_k(\epsilon)\eta^k=\eta^kQ=\overline{\eta}^kQ_1+\epsilon\left(\overline{\eta}^kQ_2+\tilde{\eta}^kQ_1\right)+H^k(\epsilon)$$

where $H^k(\epsilon)$ also represents the higher order term. Hence we have

$$\overline{\eta}^kQ_1=0\quad\text{and}\quad\left(\overline{\eta}^kQ_2+\tilde{\eta}^kQ_1\right)=\lambda_k^{\infty}\overline{\eta}^k, \tag{Equation 10}$$

where $\lambda_k^{\infty}=\lim_{\epsilon\to 0}\frac{\lambda_k(\epsilon)}{\epsilon}$. This implies that $\overline{\eta}^k\in null(Q_1)$, and hence we have $\overline{\eta}^k=\sum_{\ell=1}^{15}c_\ell^k\nu^\ell$ for some constants c_ℓ^k, where $\nu^\ell\in\mathbb{R}^{30}_{\geq 0}$ are the basis vectors of $null(Q_1)$ such that

$$\frac{\nu^\ell(\ell+15)}{\nu(\ell)}=\frac{\kappa_{on}}{\kappa_{off}}\quad\textit{and}\quad\nu^\ell(i)=0\quad\textit{for each}\ i\notin\ell,\ell+15. \tag{Equation 11}$$

Hence (9) holds.

Now we show that there exists η^k such that $c_\ell^k>0$ for each ℓ so that $\eta^k(i)=O(1)$ for each $i=1,2,\ldots,13$. Note that the biggest non-zero eigenvalue should be one of the $\lambda_k(\epsilon)$'s for sufficiently small ϵ because $\lambda_k(\epsilon)\to 0$, as $\epsilon\to 0$ and all the eigenvalues are non-positive. Since (X,N) admits absorbing states, Theorem 8 in Méléard and Villemonais (2012) implies that the eigenvector η^k associated with the biggest non-zero eigenvalue $\lambda_k(\epsilon)$ is the quasi-stationary distribution such that $\eta^k(15)=\eta^k(30)=0$, $\sum_{i=1}^{30}\eta^k(i)=1$, $\eta^k(i)\geq 0$ for each i, and for any initial distribution μ

$$\eta^k(i) = \lim_{t\to\infty} P_\mu((X(t),N(t)) = \mathbf{n}|\ \tau > t) \quad \textit{for the i th state } \mathbf{n},$$

where τ is the first absorption time of (X,N).

Without loss of generality, we let η^1 be the left eigenvalue of Q associated with the biggest non-zero eigenvalue. Then $\eta^1 = \overline{\eta}^1 + \epsilon\tilde{\eta}^1 + h^1(\epsilon)$ and $\overline{\eta}^1 = \sum_{\ell=1}^{15} c_\ell^1 \nu^\ell$ for some c_ℓ as we showed above. To show that $\eta^1(i) = O(1)$ for each $i = 1,2,\ldots,14$, it is now sufficient to prove that $c_\ell^1 > 0$ for each ℓ becasue of (Equation 11). Let E be a 30×30 such that for 15×15 identity matrix I,

$$E = \begin{pmatrix} I & I \\ I & I. \end{pmatrix}$$

Then $Q_1 E = 0$. By multiplying E to the second equation in (Equation 10) from right, we have

$$\overline{\eta}^1 (Q_2 E - \lambda_1^\infty E) = 0.$$

Let $\overline{Q} = Q_2 E - \lambda_1^\infty E$. By investigating the entries of $\overline{\eta}^1 \overline{Q}$, it follows that

$$\begin{aligned} \overline{Q}_{1,1}\overline{\eta}_1^1 + \overline{Q}_{2,1}\overline{\eta}_2^1 &= 0 \\ \overline{Q}_{i-1,i}\overline{\eta}_{i-1}^1 + \overline{Q}_{i,i}\overline{\eta}_i^1 + \overline{Q}_{i+1,i}\overline{\eta}_{i+1}^1 &= 0 \quad \text{for each } i = 2,3,\ldots,14, \end{aligned} \tag{Equation 12}$$

where $Q_{2,1} > 0$ and $Q_{i-1,i} > 0$ and $Q_{i+1,i} > 0$ for $i = 2,\ldots,14$. Suppose $\overline{\eta}_i^1 = 0$ for some $i \in \{1,2,\ldots,14\}$. Then we can derive recursively that $\overline{\eta}^i = 0$ for all $i \in \{1,2,\ldots,14\}$ because of Equation (12), and thus $\eta^1 = \tilde{\eta}^1 + h^1(\epsilon)$. This contradicts to $\eta^1(15) = \eta^1(30) = 0$ and $\sum_{i=1}^{30} \overline{\eta}_i^1 = 1$. Consequently, $\overline{\eta}_i^1 > 0$ for all $i = 1,2,\ldots,15$ and in turn $c_\ell^1 > 0$ for all $\ell = 1,2,\ldots,14$.

In the same way, we can prove the same result in Lemma 1.2 for right eigenvectors of Q. This implies that $q_1 > 0$ in (Equation 8) because q_k are the first entries of the right eigenvectors of Q as shown in (Equation 4). Therefore, letting $\lambda_1(\epsilon)$ denote the biggest non-zero eigenvalue of Q, we apply the result of Lemma 1.2 to the decomposition (8). Then assuming t is large, we have by (Equation 11) that for $i \in \{1,2,\ldots,14\}$

$$\lim_{\epsilon\to 0}\frac{p(i+15,t)}{p(i,t)} \approx \lim_{\epsilon\to 0}\frac{\sum_{k=1}^m q_k \eta^k(i+15)e^{-\lambda_k(\epsilon)t}}{\sum_{k=1}^m q_k \eta^k(i)e^{-\lambda_k(\epsilon)t}} = \lim_{\epsilon\to 0}\frac{\sum_{k=1}^m q_k \overline{\eta}^k(i+15)}{\sum_{k=1}^m q_k \overline{\eta}^k(i)}$$

$$= \lim_{\epsilon\to 0}\frac{\sum_{k=1}^m q_k \sum_\ell^{15} c_\ell^k \nu^\ell(i+15)}{\sum_{k=1}^m q_k \sum_\ell^{15} c_\ell^k \nu^\ell(i)} = \lim_{\epsilon\to 0}\frac{\sum_{k=1}^m q_k c_i^k \nu^i(i+15)}{\sum_{k=1}^m q_k c_\ell^k \nu^\ell(i)}$$

$$= \frac{\kappa_{on}}{\kappa_{off}},$$

where the limit is well-defined because $q_1 > 0$ and $c_\ell^1 > 0$ for each ℓ. For $n \in \{0,1,\ldots,13\}$, let $(n,0)$ and $(n,1)$ be the i th and $i+15$ the states, respectively. Then we finally have that for ϵ small enough

$$\frac{P(X(t),N(t)) = (n,0))}{P(X(t)=n)} = \frac{p(n,t)}{p(n,t)+p(n+15,t)} \approx \frac{1}{1+\frac{\kappa_{on}}{\kappa_{off}}} = BF,$$

and

$$\frac{P(X(t),N(t)) = (n,1))}{P(X(t)=n)} = \frac{p(n+15,t)}{p(n,t)+p(n+15,t)} \approx \frac{1}{1+\frac{\kappa_{off}}{\kappa_{on}}} = 1 - BF.$$

Therefore, by Equation (7)

$$P(X(t+\Delta t) = n-1|X(t) = n) \approx (b_n BF + d_n(1-BF))\Delta t. \tag{Equation 13}$$

Note that $b_n BF + d_n(1-BF) \in [d_n, b_n]$. The similarity of the original and the reduced models are exhibited in Figure S7.

Comparison of one-sided and two-sided nucleosome unwrapping models

In the main text, we mainly consider the stochastic nucleosome model with single-sided unwrapping, based on previously reported evidence in the literature. Here, we analyze a similarity between the original one-sided unwrapping model 1 and the two sided unwrapping model (Figures S1A and S1B). Let $X(t)$ and $\tilde{X}(t) = (\tilde{X}_1(t), \tilde{X}_2(t))$ be the stochastic DNA dynamics of the one-sided and two-side unwrapping models, respectively. The entries $\tilde{X}_1(t)$ and $\tilde{X}_2(t)$ represent the number of dissembled DNA-histone contact sites unpacked from the left edge and the right edge, respectively as $X(t)$ in the one-sided unwrapping model. Recall that for the one-sided model, when $X(t) = n$, the unwrapping and the rewrapping rates are $a_n = a_1 h^{n-1}$ and $b_n = b_1 h^{-n+1}$, respectively. In the same way, when $\tilde{X}_1(t) = n$ and $\tilde{X}_2(t) = m$, the unwrapping rate from the left edge and the right edge are $a_n^{\text{left}} = a_1^{\text{left}} h^{n-1}$ and

$a_m^{\text{right}} = a_1^{\text{right}} h^{m-1}$, respectively. Similarly, the rewrapping rate from the left edge and the right edge are $b_n^{\text{left}} = b_1^{\text{left}} h^{-n+1}$ and $b_m^{\text{right}} = b_1^{\text{right}} h^{-m+1}$, respectively. When the total number of the unwrapped regions is 14, that is $\tilde{X}_1(t) + \tilde{X}_1(t) = 14$, the process stops. In summary,

$$P(\tilde{X}_1(t+\Delta t) = n+1 | \tilde{X}_1(t) = n) = a_n^{\text{left}} 1_{\{\tilde{X}_1(t)+\tilde{X}_2(t)<14\}}$$

$$P(\tilde{X}_1(t+\Delta t) = n-1 | \tilde{X}_1(t) = n) = b_n^{\text{left}} 1_{\{\tilde{X}_1(t)>0\}}$$

$$P(\tilde{X}_2(t+\Delta t) = m+1 | \tilde{X}_2(t) = m) = a_m^{\text{right}} 1_{\{\tilde{X}_1(t)+\tilde{X}_2(t)<14\}}$$

$$P(\tilde{X}_2(t+\Delta t) = m-1 | \tilde{X}_2(t) = m) = b_m^{\text{right}} 1_{\{\tilde{X}_2(t)>0\}}$$

See Figures S1A and S1B for a description of the Markov chain associated with the two sided model.

Similarity in qualitative behaviors of the one-sided model and the two-sided model. In this section, we compare the two proposed models and prove mathematically that the two-sided model has qualitatively the similar behavior to the one-sided model. The main idea is that the left edge $\tilde{X}_1$ and the right $\tilde{X}_2$ are independently unwrapping and rewrapping until the nucleosome is fully evicted. This implies that $\tilde{X}_1(t) + \tilde{X}_2(t)$ behaves in the same way as the one-sided model does given the event of full nucleosome eviction has not yet occurred.

We prove this idea rigorously by using the random time representation proposed in (Kurtz, 1980). The Markov models $X(t)$, $\tilde{X}_1(t)$ and $\tilde{X}_2(t)$ can be represented with independent Poisson processes as

$$\tilde{X}_1(t) = \tilde{X}_1(0) + Y_3\left(\int_0^t a^{\text{left}}_{\tilde{X}_1(s)+1} 1_{\{\tilde{X}_1(s)+\tilde{X}_2(s)<14\}} ds\right) - Y_4\left(\int_0^t b^{\text{left}}_{\tilde{X}_1(s)} 1_{\{\tilde{X}_1(s)>0\}} ds\right),$$

$$\tilde{X}_2(t) = \tilde{X}_2(0) + Y_5\left(\int_0^t a^{\text{right}}_{\tilde{X}_2(s)+1} 1_{\{\tilde{X}_1(s)+\tilde{X}_2(s)<14\}} ds\right) - Y_6\left(\int_0^t b^{\text{right}}_{\tilde{X}_2(s)} 1_{\{\tilde{X}_2(s)>0\}} ds\right),$$

where Y_i's are independent unit Poisson processes. To fairly compare the two models, we set $a_n^{\text{left}} = a_n^{\text{left}} = a_n/2$ as $\tilde{X}_1(t)$ and $\tilde{X}_2(t)$ can simultaneously unwrap. In the same sense, we set $b_n^{\text{left}} = b_n^{\text{left}} = b_n/2$. By combining two independent Poisson processes we obtain

$$\tilde{X}_1(t) + \tilde{X}_2(t) = \tilde{X}_1(0) + \tilde{X}_2(0) + Y_7\left(\int_0^t \left(a^{\text{left}}_{\tilde{X}_1(s)+1} + a^{\text{right}}_{\tilde{X}_2(s)+1}\right) 1_{\{\tilde{X}_1(s)+\tilde{X}_2(s)<14\}} ds\right)$$

$$- Y_8\left(\int_0^t W b^{\text{left}}_{\tilde{X}_1(s)} 1_{\{\tilde{X}_1(s)>0\}} + b^{\text{right}}_{\tilde{X}_2(s)} 1_{\{\tilde{X}_2(s)>0\}} ds\right).$$

Recall that $a_n = a_1 h^{n-1}$ and $b_n = b_1 h^{-n+1}$. We suppose that $h = (1+\epsilon)$ with a small constant $\epsilon > 0$ to consider mildly cooperative rates. Then for $\tilde{X}_1(t) = n$ and $\tilde{X}_2(t) = m$, we can approximate the sum of two rates as

$$a_n^{\text{left}} + a_m^{\text{right}} = \frac{a_n + a_m}{2} \approx a_1 + a_1(n+m-2)\frac{\epsilon}{2} \approx a_1 \tilde{h}^{n-1+m-1},$$

$$b_n^{\text{left}} + b_m^{\text{right}} = \frac{b_n + b_m}{2} \approx b_1 - b_1(n+m-2)\frac{\epsilon}{2} \approx b_1 \tilde{h}^{-n+1-m+1},$$

where $\overline{h} = 1 + \frac{\epsilon}{2}$. Therefore given $(\tilde{X}_1(t), \tilde{X}_2(t)) \notin \{(n,m) : nm = 0, n+m = 14\}$, the total number of the dissembled contact sites $\tilde{X}_1(t) + \tilde{X}_2(t)$ can be approximated with a one-sided model

$$X(t) = X(0) + Y_1\left(\int_0^t \overline{a}_{X(s)+1} 1_{\{X(t)<14\}} ds\right) - Y_2\left(\int_0^t \overline{b}_{X(s)+1} 1_{\{X(s)>0\}} ds\right),$$

where the unwrapping rate $\overline{a}_n = a_1 \overline{h}^{n-2}$ and the rewrapping rate $\overline{b}_n = b_1 h^{-n+2}$ Thus the two models have a similar qualitative behavior. Note that if $\epsilon = 0$, the both models have the same representation as long as the nucleosome has not been fully evicted and either edge is fully wrapped. This similarity is displayed in Figures S1C and 4A in the main text as we can see the similar full eviction probability profiles of both models.

Quantitative difference between the one-sided model and the two-sided model. However, even if two models have similar qualitative dynamical behaviors, the mean of $X(t)$ and $\tilde{X}(t)$ are notably different as shown Figure S1D. This difference is mainly caused by the boundary effect. From the fully wrapped state ($X(0) = 0$ and $\tilde{X}_1(0) + \tilde{X}_2(0) = 0$), two models have the same probability to unwrap by one step. After one step unwrapping, the one-sided model is at state 1, and the two-sided model is at either $(1,0)$ or $(0,1)$.

At those states, the closing probabilities for X and $\tilde{X}_1+\tilde{X}_2$ are b_1 and $\frac{b_1}{2}$, respectively. This slight disparity in the closing probability is present whenever a single edge is closed, and the other side is open for the two-sided wrapping model, i.e. $\tilde{X}_1+\tilde{X}_2=n$ with $(\tilde{X}_1,\tilde{X}_2)=(n,0)$ or $(0,n)$. This disparity causes a longer time for the one-sided model to fully open than for the two-sided model. Even for higher fold change between two models such as $\tilde{a}_n=\frac{a_n}{4}$ and $\tilde{b}_n=\frac{b_n}{4}$, the two-sided model has a greater mean accessibility after $t=500$ as shown in Figure S1D.

Mathematical analysis for chromatin responses to different SDTF dynamics

In Section 3.1 and 3.2 of the main text, we described the dynamics of DNA with a success-failure game under oscillatory SDSTF inputs to show that various responses of DNA can be induced with different SDTF input dynamics and the system parameters. In this section, we provide more details of this description and analyze the various responses of the system under different SDTF inputs.

Rapid oscillation vs. slow oscillation. In this section, we study the response of our stochastic nucleosome model to an oscillatory SDTF signal with different frequencies. As in STAR Methods Section 1.1, we assume that the SDTF dynamics is a binary oscillation with the half-period T_0 as shown in Figure 2B of the main text so that

$$\kappa_{on}(t)=\begin{cases}\kappa_{on} & \text{if } t\in[2mT_0,(2m+1)T_0) \text{ for some m}\\ 0 & \text{if } t\in[(2m-1)T_0,2mT_0) \text{ for some m,}\end{cases} \quad \text{(Equation 14)}$$

and we set $\kappa_{on}=100$ and $\kappa_{off}=42.85$ so that $BF=\frac{\kappa_{off}}{\kappa_{off}+\kappa_{on}}=0.3$.

For simplicity, we first consider the case that the cooperativity constant $h=1$. We also assume that $b_n=ca_n$ with $c>1$ large and $d_n=0$ for each n, which means that DNA rarely unwraps without SDTF binding as b_n is much greater than a_n for all n. Let $T_{on,m}=(2m-1)T_0$ and $T_{off,m}=2mT_0$ for $m=1,2,\ldots$. Then by considering conditional probabilities, we have

$$\begin{aligned}P\left(X_{T_0}(T_{off,n})=14\right)&=P\left(X_{T_0}(T_{off,n})=14\middle|X_{T_0}(T_{off,n-1})=14\right)P\left(X_{T_0}(T_{off,n-1})=14\right)\\&+P\left(X_{T_0}(T_{off,n})=14\middle|X_{T_0}(T_{off,n-1})<14\right)P\left(X_{T_0}(T_{off,n-1})<14\right)\end{aligned} \quad \text{(Equation 15)}$$

To simplify (15), we approximate two quantities. First, due to $b_n>a_n$ the DNA dynamics $X_{T_0}(t)$ rarely reaches state 14 during the off-phase $[T_{on,m},T_{off,m}]$ where $\kappa_{on}(t)=0$. Hence $P(X_{T_0}(T_{off,n-1})=14)\approx P(X_{T_0}(T_{on,n-1})=14)$. Secondly, for the same reason the DNA dynamics X_{T_0} steps back to state 0 during the off-phases with high probability as described in Figure 2C of the main text. Therefore we have approximately that

$$P\left(X_{T_0}(T_{off,n})=14\middle|X_{T_0}(T_{off,n-1})<14\right)\approx P\left(X_{T_0}(T_{off,n})=14\middle|X_{T_0}(T_{off,n-1})=0\right)$$

$$=P\left(X_{T_0}(2T_0)=14\right)\approx P\left(X_{T_0}(T_0)=14\right).$$

Finally, since state 14 is an absorbing state, the probability $P(X_{T_0}(T_{off,n})=14|X_{T_0}(T_{off,n-1})=14)$ is 1. Denoting $P(X_{T_0}(T_0)=14)=\rho_{T_0}$, therefore, we approximate $P(X_{T_0}(T_{off,n})=14)$ as

$$P\left(X_{T_0}(T_{off,n})=14\right)\approx P\left(X_{T_0}(T_{off,n-1})=14\right)+\rho_{T_0}P\left(X_{T_0}(T_{off,n-1})<14\right)$$

$$=\rho_{T_0}+(1-\rho_{T_0})P\left(X_{T_0}(T_{off,n-1})=14\right)$$

Hence we inductively derive that

$$P\left(X_{T_0}(T_{off,n})=14\right)\approx\sum_{i=1}^{n}\rho_{T_0}(1-\rho_{T_0})^{i-1}=P\left(Geo(\rho_{T_0})\le n\right), \quad \text{(Equation 16)}$$

where $Geo(\rho_{T_0})$ is a random variable following the geometric distribution with success probability ρ_{T_0}. Therefore the full eviction probability can be described as a success-failure game (Figure S2A).

The full eviction probability by 500 min under the rapid oscillation is approximately

$$Prob(X(500)=14)\approx Prob(Geo(0.025)\le 25)=\sum_{i=1}^{25}0.025(1-0.025)^{i-1}=0.47.$$

Hence for an SDTF signal that turned on and off repeatedly every 10 min, about 47% of chromatin became accessible at 500 min (Figures 2B and 2C).

On the other hand, if the SDTF signal was maintained for 60 min, about 24% of DNA reached state 6 (Figure S2C). Although DNA rapidly rewraps over the next off-phase of the SDTF signal, once the SDTF is active again for the next 60 min, about 24 % of remaining DNA became unwrapped. Through the success-or-failure game 4 times within [0.500] min, about $70\%=Prob(Geo(0.24)\le 4)\times 100\%=\sum_{i=1}^{4}0.24(1-0.24)^{i-1}\times 100\%$ of DNA became fully unwrapped (Figures 2B and 2C).

For $h>1$, the rates a_n and b_n are cooperative so that there exists N such that $a_{n+1}\ge b_n$ for each $n\ge N$. In this case, we consider the probability of reaching a state $\ge N$ by time $T_{off,n}$ instead of state 14 because once X_{T_0} reaches state N or goes further, then $X_{T_0}(t)$ likely

reaches state 14 quickly even though $N(t) = 0$ due to a_{n+1} is much bigger than b_n for $n \geq N$. Hence we let τ_N be the first hitting time of state N, and let also $\rho_{N,T_0} = P(\tau_N < T_0)$. That is, ρ_{N,T_0} means the probability of hitting state N within $[0,T_0)$. As shown above, hence, we approximate the full eviction probability as

$$P(X_{T_0}(T_{\text{off},n}) = 14) \approx P(X_{T_0}(T_{\text{off},n} \geq N) = P(\tau_N < T_{\text{off},n})$$

$$= P(\tau_N < T_{\text{off},n-1}) + \rho_{N,T_0} P(\tau_N > T_{\text{off},n-1})$$

$$= \sum_{i=1}^{n} \rho_{N,T_0}(1 - \rho_{N,T_0})^{i-1} = P(Geo(\rho_{N,T_0}) \leq n),$$

Figure S2B illustrate this approximation under oscillatory inputs with various half-periods. The quantify ρ_{N,T_0} can be easily computed with $\mu e^{Q_{\text{on}} T_0}$ as shown in Equation (5). We display the plot of ρ_{N,T_0} as a function of T_0 in Figure S2C.

The success-failure game scheme is valid due to $b_n > a_n$ for most states with large constant c such that $b_1 = ca_1$. Therefore when the constant c is small, the approximation (16) may be inaccurate as shown in Figure S2D. Furthermore, if the oscillation is too fast, DNA cannot read the oscillation so that the success-failure game scheme is also invalid because the approximation scheme relies on the oscillation of $\kappa_{\text{on}}(t)$ (Figure S2E). In the same sense, if the rates a_n and b_n are too small, then the expected transition time of $X(t)$ is too long so that the success-failure scheme does not accurately approximate the full eviction probability (Figure S2F).

As described in Section 3.1 of the main text, if the SDTF oscillation is extremely fast, the oscillatory input is approximately decoded as a constant signal. This can be simply shown with the probability density functions. Let $N_\ell(t)$ and $N_\infty(t)$ be continuous-time Markov chain defined on $\{0,1\}$. For $N_\ell(t)$, the transition rate from 0 to 1 is $\kappa_{\text{on}}(t)$ defined in (Equation 14) with $T_0 = \frac{1}{\ell}$. For $N_\infty(t)$, the transition rate from 0 to 1 is constant at $\kappa/2$. For both processes, the transition rate from 1 to 0 is κ_{off}. These processes represent the SDTF binding and unbinding under an oscillatory signal and a constant signal, respectively. Note that the temporal average of the oscillatory signal is $\frac{1}{t}\int_0^t \kappa_{\text{on}}(s)ds = \kappa/2$. Since the state space consists of only two states, we can explicitly find the probability density function for $N_\ell(t)$ and $N_\infty(t)$. Let $p_\ell(t)$ and $p(t)$ be the probability of N_ℓ and N_∞ being at state 1 at t, respectively. Then assuming both processes starting at 0, we have

$$p(t) = \frac{\kappa}{2\kappa + \kappa_{\text{off}}}\left(1 - e^{-(\kappa/2 + \kappa_{\text{off}})t}\right),$$

$$p_\ell(t) = \frac{1}{e^{(\kappa/2+\kappa_{\text{off}})t}}\left(\int_0^t e^{(\kappa/2+\kappa_{\text{off}})s}\kappa/2ds + \int_0^t e^{(\kappa/2+\kappa_{\text{off}})s}(\kappa_{\text{on}}(s) - \kappa/2)ds\right)$$

$$= p(t) + \int_0^t e^{(\kappa/2+\kappa_{\text{off}})s}(\kappa_{\text{on}}(s) - \kappa/2)ds,$$

Since the integration $\int_0^t e^{(\kappa/2+\kappa_{\text{off}})s}(\kappa_{\text{on}}(s) - \kappa/2)ds$ tends to 0, as $\ell \to \infty$, we have $\lim_{\ell\to\infty} p_\ell(t) = p(t)$ for each t. Hence for an extremely fast oscillation of the SDTF inputs, the SDTF binding/unbinding can be approximated with the constant SDTF signal whose input level is the temporal average of the oscillation. Figure S2G is the full eviction probability as a function of T_0 in a log scale.

Chromatin dynamics with cell heterogeneity under oscillatory SDTF signals. Cells are often heterogeneous so that the same system in different single cells admits various range of parameters. Depending on the system structure, the outcome can be robust to the parameters and inputs (Kim and Enciso, 2020; Shinar and Feinberg, 2010; Shoval et al., 2010; Stelling et al., 2004). On the contrary, the output can be significantly influenced by even tiny change of system parameters or inputs. This refers to sensitivity of the system. In Section 3.2 of the main text, we showed that the stochastic epigenome model is sensitive to the unwrapping/rewrapping parameters, and the sensitivity can be amplified by an oscillation of the SDTF input signal. In this section, we show that how this sensitivity can be caused by oscillation with more detailed analysis.

As in STAR Methods Section 3.1, we set $b_1 = ca_1$ with $c > 1$ large. We further assume that the cooperativity constant $h \geq 1$ is close to 1. For the given unwrapping/rewrapping parameters a_n and b_n, we consider x-fold change as $a_n(x) = a_n x$ and $b_n(x) = b_n x$ to explore the sensitivity of the system in x. Let $X_{os}(t)$ be the DNA dynamics under the oscillatory signal $\kappa_{\text{on}}(t)$ defined in Equation (14). Let $\rho_{\text{os}} = P(X_{os}(T_0) = N)$ where N is the state such that $a_{n+1} \geq b_n$ for all $n \geq N$. Then as described in STAR Methods Section 3.1, for $T = 2mT_0$ the full eviction probability is

$$P(X_{os}(T) = 14) \approx \rho_{\text{os}} + \rho_{\text{os}}(1 - \rho_{\text{os}}) + \cdots + \rho_{\text{os}}(1 - \rho_{\text{os}})^{m-1} = P(Geo(\rho_{\text{os}}) \leq m),$$

where each term $\rho_{\text{os}}(1 - \rho_{\text{os}})^\ell$ is the probability of X reaching state 14 within the phase $[2\ell T_0, (2\ell+1)T_0]$ after ℓ times failures in the previous on-phases. On the contrary to the case of oscillatory SDTF signals, for the DNA dynamics $X_{const}(t)$ under a constant signal $\kappa_{\text{on}} = 50$, the probability of reaching state 14 at $T = 2mT_0$ can be express as a single success-failure game for a longer time as

$$P(X_{\text{const}}(T) = 14) \approx P(X_{\text{const}}(T) = N) = \rho_{\text{const}} = P(Geo(\rho_{\text{const}}) = 1).$$

The polynomial $f_m(\rho) = \sum_{i=1}^{m} \rho(1-\rho)^{i-1}$ have distinct sensitivity to the value of ρ (Figure S3H) for each m. Note that $P(X_{os}(T) = 14) \approx f_m(\rho_{os})$ and $P(X_{const}(T) = 14) \approx f_1(\rho_{const})$. This describes how the oscillation causes the sensitive response of the DNA full eviction to the parameter change.

In Figure 2F of the main text, we showed that the sensitivity is induced by an oscillatory input under cooperativity $h = 1.3$ when $\frac{b_1}{a_1} = 15$. If this ratio is not that big, for example $\frac{b_1}{a_1} = 7$, then although the system is mildly cooperative with $h = 1.1$ the sensitivity is still induced with the oscillatory inputs as shown in Figure S2I.

Studying the system parameters with the SDTF binding site effect

In this section, we explore the optimal binding site of SDTF for unwrapping DNA from a nucleosome under different cooperativity relationship among the unwrapping and rewrapping rates. For simplicity, we assume that the SDTF signal $\kappa_{on}(t)$ is constant.

Binding site effects with cooperative and non-cooperative rates. To study how the full eviction probability varies by the SDTF binding sites, we simplify the stochastic epigenome system (1) with discrete-time random walks as shown in Figure S4. To intuitively find the optimal SDTF binding site, we use the expected number of steps to reach state 14 instead of the full eviction probability at a fixed time T. Let X be an 1-dimensional random walk defined on the state space $\{0, 1, 2, \ldots, N\}$ with the transition probabilities p and q of the right-steps and left-steps, respectively. For X, let $K_{n,m}$ be the expected number of transitions to reach state m from state n. Then we can derive the following recursive relations with Markov properties:

$$K_{n-1,n} = 1 + qK_{n-2,n} = 1 + q(K_{n-2,n-1} + K_{n-1,n}).$$

This implies that

$$K_{n-1,n} = \left(\frac{q}{p}\right)^{n-1}\left(K_{0,1} - \frac{1}{p-q}\right) + \frac{1}{p-q} = \left(\frac{q}{p}\right)^{n-1}\left(1 - \frac{1}{p-q}\right) + \frac{1}{p-q},$$

since $K_{0,1} = 1$. Finally we have

$$K_{0,n} = \sum_{i=1}^{n} K_{i-1,i} = \frac{2r}{r-1}\frac{r^n - 1}{r-1} - \frac{n(r+1)}{(r-1)}, \qquad \text{(Equation 17)}$$

where $r = \frac{q}{p}$. We use this calculation to derive the expected number of transitions of the random walks in Figures S4A and S4B.

First, we find the optimal SDTF binding site under cooperative rates (i.e. both a_n and b_n are constants in the stochastic epigenome model). Under this setting, the stochastic epigenome model can be simplified as the random walks in Figure S4A where the transition probabilities p and q are constants. Each random walk has a designated state from where the backward transition is prohibited. This setting is analogous to the SDTF binding sites of our stochastic epigenome model. Let $T_{n,m}$ be the expected number of transitions to reach state m from state n of the random walks in Figure S4 with the designate state. Note that $T_{n,m}$ and $K_{n,m}$ represent different quantities as $T_{n,m}$ indicates the expected number of transitions with the designated state, while $K_{n,m}$ is defined for the random walk X without a designated state. We further assume that $r = \frac{q}{p} = 2$ to replicate the assumption that the rewrapping rate is higher than the unwrapping rate.

The random walk model in Figure S4A top has no backward step from state 4. Then

$$T_{0,14} = T_{0,4} + T_{4,14} = K_{0,4} + K_{0,10} = 4110,$$

where we note that $T_{4,14} = K_{0,10}$ as the transition from state 4 to state 14 is equivalent to the transition from state 0 to state 10 of X. The random walk in Figure S4A bottom has no backward step from state 7, which corresponds to the SDTF binding at dyad. Then

$$T_{0,14} = T_{0,7} + T_{7,14} = 2 * K_{0,7} = 974.$$

In the same way, we can compute $T_{0,14}$ with different SDTF binding sites as shown in Figure S4C, which indicates that binding at the center more efficiently help unwrapping DNA than binding at the edge.

Now, we consider the random walks in Figure S4B that estimate the behavior of the stochastic epigenome model under cooperative parameters. For simplicity, we assume that there are two types of unwrapping and rewrapping rates such that for some $\ell \in \{0, 1, 2, \ldots, 14\}$

$$q_i = rp_i \quad \text{for } i \le \ell \quad \text{and} \quad q_i = r'p_i \quad \text{for } i > \ell$$

with some r and r'. To replicate the cooperativity assumed in the main text, we suppose that $r = 2$ and $r' = 0.5$ so that the random walker steps forward more easily around the right-edge than around the left-edge. As we define previously, for the random walks in Figure S4B, we define $T_{n,m}$ as the expected number of transitions to state m from state n. We also assume that $\ell = 7$ and hence the unwrapping rate is greater than the rewrapping rate for all states in $\{7, 8, \ldots, 14\}$.

For the random walk in Figure S4B top, we can compute $T_{0,14}$ by decomposing it as $T_{0,14} = T_{0,4} + T_{4,7} + T_{7,14}$. Computing $T_{7,14}$ is complicated as we need to consider the mixture of the transition probabilities $q_i = 2p_i$ and $q_i = 0.5p_i$. By using the same recursive relation shown above, we have

$$T_{7,8} = 1 + q_6 T_{6,8} = 1 + q_6(T_{6,7} + T_{7,8}).$$

This implies that $p_6T_{7,8} = 1 + q_6T_{6,7}$ and hence $T_{7,8} = 28$, where we note that $T_{6,7} = K_{2,3} = 13$. By doing so, we can recursively compute $T_{8,9} = 16, T_{9,10} = 9.5, T_{10,11} = 6.25, T_{11,12} = 4.625, T_{12,13} = 3.8125$ and $T_{13,14} = 3.40625$ in the same way. Therefore $T_{7,14} = \sum_{i=8}^{14} T_{i-1,i} = 2.59375$ and hence

$$T_{0,14} = T_{0,4} + T_{4,7} + T_{7,14} = K_{0,4} + K_{0,3} + T_{7,14} = 139.59375.$$

In the same way, we compute $T_{0,14}$ of the random walk in Figure S4B bottom as

$$T_{0,14} = K_{0,7} + T_{7,14} = 504.03125,$$

which is greater than $T_{0,14}$ of the SDTF binding site at state 4. On contrary to the case of non-cooperative rates, therefore, when the unwrapping and rewrapping rates are cooperative as we assumed above, the SDTF binding at dyad is not the optimal binding site for full eviction.

We can generalize the computation of $T_{0,14}$ with different values of ℓ, and we can use this to test how the optimal SDTF binding sites vary with the degree of cooperativity. The solid and dotted plots in Figure S4D show that $T_{0,14}$ under highly cooperative rates ($\ell < 6$) and mildly cooperative rates ($\ell \geq 7$), respectively. As the plots show, the optimal binding sites are located toward the left-edge when the rates are more cooperative.

Predict the system parameters. By using the random walk models to simplify the original stochastic epigenome model, we proved in STAR Methods Section 4.1 that the full eviction probability of DNA varies in the SDTF binding sites so that the full eviction probability profile exhibits a special pattern as shown in Figure 4A of the main text. We further showed that this pattern can be considerably varied under different degree of cooperativity and the range of the SDTF binding effect.

This probability profile allows us to predict the system parameter by comparing the computational results to the experimental location-specific measurements. Let x be the relative distance between the SDTF binding site and dyad. Let further $p(x)$ be the average full-eviction probability for the distance x. First of all, as the optimal binding sites vary in different degree of cooperativity, we recognize that the width of the center dip appearing in the probability profile differs in the cooperativity parameter h. Since the optimal binding sites tend to move to the edges (state 0 or state 14), the width of the center dip increases as h increases in the plot of $p(x)$ (Figure S5A the 1st panel).

We can also predict the effects of other parameters. As the opening rate a_1 increases, $p(x)$ across all the range of the distance x translates up. Similarly, as the close rate b_1 decreases, $p(x)$ also translates up (Figure S5A the 2nd panel). The parameter $BF = \frac{k_{\text{off}}}{k_{\text{off}} + k_{\text{on}}}$, the ratio of the SDTF binding and unbinding rates, controls the magnitude of the SDTF binding effect. The rewrapping rates lying the range of the SDTF effect decreases when BF increases as shown in (Equation 13), which in turn induces sharper peaks in the probability profile (Figure S5A the 3rd panel). Range of the SDTF effect, determined with the constant σ in $d_n = b_n\left(1 - e^{\frac{1}{2}\left(\frac{n-s}{\sigma}\right)^2}\right)$, is also one of the critical parameters for special pattern in the plot of $p(x)$. For short range of the SDTF effect, the full eviction probability dramatically changes for each binding site. This causes that the depth of the center dip becomes dipper as shown in the 4th panel of Figure S5A. Furthermore, an SDTF binding site with long distance to dyad does not affect the system if the range σ is too small. Thus if σ is too small, a plateau appears in the plot of $p(x)$ around x such that $|x|$ is big.

From a given ATAC-seq measurement for the change of the nucleosome counts with a certain SDTF binding motif location (Figure S5B), we can calculate $p(x)$ and plot it. Then by using the fact that each parameter of the stochastic epigenome system characterizes $p(x)$, we can make an initial guess of the parameter values comparing to the experimentally measured $p(x)$. And then as described in Figure S5C, we can further tune the parameters for more accurate fitting with the gradient decent searching algorithm, which is a typical algorithm for searching optimal system parameters. We use L^2 norm to define the loss function for the gradient decent algorithm as $d = \sum_{i=1}^{m} |p_0(i) - p(i)|^2$, where i indicates the i SDTF binding location, p_0 is the experimentally measured full eviction probability, and p is the full eviction probability computed with the stochastic model. The plots in Figure S5D display that the fitted parameters are actually global optimization values of the L^2 distance.

Modeling under generalized parameter sets

Continuity of the stochastic nucleosome model. Here we state that the statistical quantities associated with the stochastic nucleosome model is almost preserved under small variations to the model parameters since the probability density function is continuous in the model parameters. To visualize this, we add small noise to the unwrapping/rewrapping parameters, and show how the full eviction probabilities change.

First of all, to incorporate noise in the unwrapping and rewrapping parameters, a_n and b_n, we add a Gaussian noise to the parameters so that the new noisy parameters are $\tilde{a}_n = a_n + Z_{1,n} + \tilde{a}_n = a_n + Z_{2,n}$, where $Z_{i,n}$ is a normal random variable with mean 0 and variance $a_n/10$ and $b_n/10$, respectively for $i = 1$ and 2. In case some parameter becomes negative, we make it zero. Then we obtain the Eviction Probability Profiles of the stochastic model under both non-cooperative setting and cooperative setting. The noise added to a_n and b_n can continuous; y deform the eviction probability profiles (Figure S6A). As the original setting without noise in the parameters, therefore, the unique characteristic of the Eviction Probability Profiles is preserved with a single peak for the non-cooperative case and double peaks for the cooperative case (Figure S6B). This variability of a_n and b_n can be associated with the variability of the DNA-histone affinity caused by DNA sequence. Secondly, we allow an event of rebinding of DNA to a histone after full eviction

with small probability as described in Figure S6C. Then the continuity of the full eviction probability guarantees the geometric characteristic of the Eviction Probability Profile is preserved with this small variation (Figure S6D).

Dependence of binding/unbinding rates on the binding motif location. Recall that the binding/unbinding rates κ_{on} and κ_{off} are independent of the binding location in our original model introduced in the main text. However, one can consider binding/unbinding rates depending on the binding location as the SDTF may not easily bind at more buried sites on the nucleosomal DNA. Thus we can use $\kappa_{on}(s)$ and $\kappa_{off}(s)$ for the binding/unbinding rate, respectively as functions of the binding location $s \in \{0, 1, \ldots, 14\}$.

First, we can assume that $\kappa_{on}(s)$ follows the upside-down Gaussian curve as shown in the right panel of Figure 5A so that the SDTF has the lowest binding rate at dyad. We can further assume that the binding and unbinding are equally hard for buried sites so that for all s, the ratio $\frac{\kappa_{on}(s)}{\kappa_{off}(s)} = r$ for some constant r. We showed in STAR Methods Section 1.2 that the model behavior solely depends on $BF = \frac{\kappa_{off}(s)}{\kappa_{on}(s)+\kappa_{on}(s)} = \frac{1}{r+1}$ rather than the individual $\kappa_{on}(s)$ and $\kappa_{off}(s)$. Hence although the binding/unbinding rates are varied with the binding location s, the stochastic nucleosome model under $\kappa_{on}(s)$ and $\kappa_{off}(s)$ has the same behavior as the original model under the binding location-independent binding/unbinding rates. Despite the ratio between $\kappa_{on}(s)$ and $\kappa_{off}(s)$ are not identical across all the binding sites s, the Eviction Probability Profiles have the same qualitative patterns when the variation of the ratio is not substantial (Figure 5B). This was theoretically verified with the continuity of the eviction probability described as in STAR Methods Section 5.1.

Alternatively, we can also assume that the binding rate is a function of the DNA opening states, $X(t)$. It is possible that when an SDTF binding site is exposed by DNA opening, the SDTF binding rate is higher than the binding rate when the binding site is buried by a wrapped nucleosome status. To model this, we assume that $\kappa_{on}(n)$ and $\kappa_{off}(n)$ are functions of the DNA opening state n as described in the right panel of Figure 5C. As long as the variability of $\kappa_{on}(n)$ and $\kappa_{off}(n)$ with respect to n is not too big, the Eviction Probability Profiles possess a consistent shape under both the non-cooperative case and the cooperative case as shown in Figure 5D.

Mean unwrapping times

In Tims et al. (2011), it was shown that the unwrapping time from DNA opening state n to $n+1$ is increasing as n increases. This means that the unwrapping rate around the dyad (or more buried sites) is lower than the unwrapping rate around the edges. This conclusion seems to conflict to our result that the DNA-histone binding affinity is cooperative so the more unwrapped DNA state the easiler further unwrapping. However, the unwrapping time measured in Tims et al. (2011) is the time for DNA to reach state $n+1$ from n. Hence there could be multiple unwrapping/rewrapping steps of DNA inbetween the final transition from n to $n+1$. For exampple, DNA can go through a sequence of steps $n \rightarrow n-1 \rightarrow n-2 \rightarrow n-3 \rightarrow n-2 \rightarrow n-1 \rightarrow n \rightarrow n+1$ for a transition from n to $n+1$. To check consistency of our work with the previous work, we also simulated our model under the cooperative setting we revealed in this research to measure the time for unwrapping from state n to state $n+1$. As shown in Figure S6F, the time increases as a function of n (Figure S6F left). Similarly, the first time for rewrapping from state n to state $n+1$ can be also measured, and it is shown that the time increases as n increase, but the increment is not as significant as the unwrapping case (Figure S6F right). These results are consistent with the results in (Tims et al., 2011).

QUANTIFICATION AND STATISTICAL ANALYSIS

Model simulations

Model implementation and simulations were performed in MATLAB 2016b. Further detailed description of the model can be found in the Method details.

Coefficients variation

The coefficient variation for a probability distribution or a random variable is calculated with the standard deviation divided with the mean. Since this quantity gives a normalized degree of variation of a given probability distribution, we can use them to compare the variabilities of two probability distributions as described in Figure 2G.

Total variation distance

We used the total variation distance to measure similarities between the distributions of chromatin accessibilities under an oscillatory signal and a constant signal shown in Figure 4E. For probability distribution P_1 and P_2 defined on the same finite state space, the total variation distance is defined as $\|P_1 - P_2\|_{tv} = max_A|P_1(A) - P_2(A)| = \frac{1}{2}\sum_x|P_1(x) - P_2(x)|$. The usage of this distance can be found in "Model predicts cooperativity based on Eviction Probability Profiles" in Results.

ATAC-seq data processing

Macrophage ATAC-seq samples were generated as previously described (Buenrostro et al., 2015), and single-end data was obtained from (Cheng et al., 2021). Macrophage ATAC-seq libraries of the IκBα knockout mouse from Cheng et al. (2021) were re-sequenced paired-end 2 × 150 on HiSeq4000. Only paired-end sequencing allows the separation of nucleosomal fragments from non-nucleosomal fragments, as read fragments with lengths shorter than the nucleosome footprint of ~150 basepairs can be classified as nucleosome-free accessible regions, while read fragments of ~150bp, or a multiple of 150bp, can be classified as accessible nucleosomal genomic regions, with cut sites flanking nucleosome boundaries. ATAC-seq fastqs were processed through the ENCODE-DCC

ATAC-seq pipeline (https://github.com/ENCODE-DCC/atac-seq-pipeline). The reads were trimmed using cutadapt, and aligned to mm10 or hg38 using bowtie2. Picard was used to de-duplicate reads, which were then filtered for high quality, paired reads using samtools. Peak calling was performed using macs2. The optimal Irreproducible Discovery Rate (IDR) thresholded peak output was used for all downstream analyses, with a threshold p-value of 0.05. Other ENCODE3 parameters were enforced with the flag –encode3. Reads that mapped to mitochondrial genes or blacklisted regions, as defined by the ENCODE pipeline, were removed. The peak files were merged using *bedtools merge* to create a consensus set of peaks across all samples.

ATAC-seq nucleosome analysis

Nucleosome positions were called using the merged regions, from paired-end ATAC-sequencing data, using the published software NucleoATAC (Schep et al., 2015). An example genomic location *Cxcl2*, illustrates the information obtained is orthogonal to simply chromatin accessibility (Figure S6). The output of this software provides putative nucleosomal and nucleosome-free regions of accessible chromatin, by analyzing the patterns of ATAC-seq read fragment sizes. As described in full detail in Schep et al. (2015), nucleosome occupancy is called by maximum likelihood estimation, and nucleosome dyad positions are called by considering the local maxima of candidate nucleosome positions. Genomic locations of nucleosome positions called were annotated, and NF-κB motifs were found using the tool HOMER (Heinz et al., 2010). Motif searching was done using the three NF-κB motif position weight matrices within the HOMER database, for length 9, 10, 11. Motifs were listed if they occurred within +/−200 basepairs of the nucleosome dyad. Nucleosomes across timepoints were matched by assigning them to their closest transcription start site for each sample. Nucleosomes assigned to a TSS for the baseline time point, and subsequently not found at that TSS at the later time point, were considered evicted. For analyses where the model calculated a probability of nucleosome eviction, nucleosomes that appeared, and matched to a new gene at the second time point but not in the first, were ignored. Probabilities of eviction p with respect to location of the binding motif and distance from nucleosome dyad were calculated by taking bins of distance from dyad, and using the following formula for each bin: $p = \frac{n_{t=0} - n_{t=4}}{n_{t=0}}$, where $n_{t=h}$ is the number of nucleosomes at h hours.